Marine and Petroleum Geology 165 (2024) 106850

Contents lists available at ScienceDirect

Marine and Petroleum Geology

journal homepage: www.elsevier.com/locate/marpetgeo

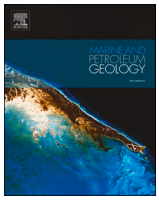

Fracture analysis and low-temperature thermochronology of faulted Jurassic igneous rocks in the Southern Colombian Andes: Reservoir and tectonic implications

Juan Camilo Valencia-Gómez [a,*], Agustín Cardona [a], Sebastián Zapata [b], Gaspar Monsalve [a], Dora Marín [c], Maryi Rodríguez-Cuevas [a], Edward R. Sobel [d], Mauricio Parra [e], Johannes Glodny [f]

[a] Grupo de Estudios en Geología y Geofísica (EGEO), Universidad Nacional de Colombia, 80 Avenue No. 65 – 223, 050034, Medellín, Colombia
[b] Group of Studies in Orogenic Systems (GROSSE), Faculty of Natural Sciences, Universidad del Rosario, 12C Street No. 6-2, 111711, Bogotá, Colombia
[c] Vår Energi, Sandnes, Norway
[d] Institute of Geosciences, University of Potsdam, Potsdam, Germany
[e] Instituto de Geociências, Universidade de São Paulo, São Paulo, Brazil
[f] GFZ German Research Centre for Geosciences, Potsdam, Germany

ARTICLE INFO

Keywords:
Volcanic reservoirs
Fracture networks
Fault damage zone
Fracture stratigraphy
Thermochronology
Northern Andes

ABSTRACT

Fractured basement hydrocarbon reservoirs are widely distributed worldwide in more than 30 basins, where volcanic and plutonic rocks have produced significant quantities of oil and gas. The Upper Magdalena Valley Basin (UMVB) is a mature and productive hydrocarbon basin located in the Colombian Andes. In this basin, plutonic and volcaniclastic Jurassic rocks are thrusted on top of Cretaceous to Cenozoic sedimentary rocks, which constitute the petroleum system. Multi-scale fracture analysis together with petrography, petrophysics, and low-temperature thermochronology were conducted in and outcrop analogue of this basement to assess the structural evolution and investigate the main factors controlling the development of fracture properties in igneous basements. Thermochronological data indicate the occurrence of three exhumation events between the Early Cretaceous and Miocene, suggesting that most of the fracture networks within the Agrado-Betania hanging-wall were likely formed before hydrocarbon migration. Structural analysis has identified a fault damage zone with a width of approximately 746 m. Volcanic breccias and ash tuffs exhibit slightly higher areal fracture intensities ($P_{21} > 30\ m/m^2$) compared to plutonic and clastic rocks ($P_{21} < 20\ m/m^2$). Furthermore, the fracture networks exhibit good connectivity, with connection per branch (C_B) values exceeding the 1.5 percolation threshold. Petrophysical calculations of matrix-fracture properties indicate high permeabilities (ranging from 1000mD to 10000000mD) and low porosities (<10%). The structural position and the diagenetic transformation of the volcanic rocks are the primary factors controlling fracture intensity in the igneous rocks within the Agrado-Betania fault. Results from this outcrop analogue also show that polyphasic structural histories and the burial history positively influence the quality of fractured basement reservoirs.

1. Introduction

Fracture attributes, including kinematic aperture, intensity, and connectivity have been related to rheology or fault deformation history. These attributes influence the structural geometries and the flow properties and the accumulation capacity of reservoir rocks (Cooke, 1997; Ferrill et al., 2017; Laubach et al., 2009, 2019; Manniello et al., 2022; Saein and Riahi, 2019; Wennberg et al., 2007). Fracture variations between different rock types have been conceptualized as "fracture stratigraphy" and can be used to understand subsurface reservoir conditions (Laubach et al., 2009). Research in fracture stratigraphy has been mostly developed on clastic and carbonate successions, which are common hydrocarbon reservoirs (Dashti and Rahimpour-Bonab, 2022; Manniello et al., 2022; Saein and Riahi, 2019; Todaro et al., 2022; Ukar et al.,

* Corresponding author.
E-mail addresses: juacvalenciagom@unal.edu.co (J.C. Valencia-Gómez), agcardonamo@unal.edu.co (A. Cardona), sebastian.zapatah@urosario.edu.co (S. Zapata), gmonsalvem@unal.edu.co (G. Monsalve), dora.marin@varenergi.no (D. Marín), marcrodriguezcue@unal.edu.co (M. Rodríguez-Cuevas), sobel@rz.uni-potsdam.de (E.R. Sobel), mparra@iee.usp.br (M. Parra), glodnyj@gfz-potsdam.de (J. Glodny).

https://doi.org/10.1016/j.marpetgeo.2024.106850
Received 15 September 2023; Received in revised form 9 March 2024; Accepted 7 April 2024
Available online 20 April 2024

2019).

Numerous studies, performed in sedimentary rocks, have demonstrated that fracture attributes are controlled by many factors, such as the position in relation to regional structures ;, tectonic stress magnitude and intensity;, long-term structural history, mechanical stratigraphy, lithological properties, diagenesis, and the pre-deformational structural configuration (Nelson and Serra, 1995; R. J. Lisle, 1994; Wennberg et al., 2007; Laubach et al., 2009, 2019; Ortega et al., 2010; Li et al., 2018; Watkins et al., 2018; Manniello et al., 2022; Mora et al., 2013; Saein and Riahi, 2019; Sánchez-Villar et al., 2011; Tamara et al., 2015; Todaro et al., 2022; Ukar et al., 2019).

Crystalline hydrocarbon reservoirs have been discovered in over 30 basins worldwide, some of which are characterized by a significant production of oil and gas (Bonter and Trice, 2019; Cuong and Warren, 2009; Koning, 2019; Sun and Zhong, 2018; Tang et al., 2022; Wen et al., 2019; Zou, 2017), reaching rates of oil production as high as 280,000 barrels of oil per day (Koning, 2019). In these basins, fractured volcanic and plutonic units have been found charged with liquid and gas (Debenham et al., 2019; Dimmen et al., 2017; Sanderson and Nixon, 2018).

Understanding the rheological and diagenetic properties that control fracturing in volcanic rocks can be challenging due to their stratigraphic heterogeneity. These units include pyroclastic facies interbedded with sedimentary rocks that are commonly associated with intrusive bodies, such as domes, sills, and dykes (Sun and Zhong, 2018; Zheng et al., 2018; Wen et al., 2019). Furthermore, rock rheology, and ultimately the fracture networks, can also be affected by rock composition (mafic to felsic) as there will be variation in the resistance of minerals to deformation in the burial and diagenetic histories (Wei et al., 2022) and in the superimposed tectonic deformation and exhumation.

Located in the southern Colombian Andes, the Upper Magdalena Valley Basin (UMVB) is the result of Mesozoic to Cenozoic sedimentation and deformation linked to the formation of the adjacent mountain belts (Fig. 1). Several NNE-SSW regional faults that bound this basin expose the volcano-plutonic basement as a result of a polyphasic structural evolution (Espitia et al., 2022; Jiménez et al., 2012; Mora et al., 2010; Rosero et al., 2022). This basin holds commercial accumulations of conventional oil and gas generally trapped in Cretaceous reservoirs, which have been exploited since 1962 (Sarmiento and Rangel, 2004). The economic basement of this basin is mainly constituted of Jurassic volcanic and plutonic rocks, which are juxtaposed against the Cretaceous source and reservoir rocks (de Freitas, 2000; Ramon and Rosero, 2006; Rosero et al., 2022; Sarmiento and Rangel, 2004), opening the possibility for hydrocarbon migration into the fractured igneous basement.

Since the Early Cretaceous, this basin has been shaped by a polyphasic tectono-structural history, which encompasses an initial extensional phase, which is superposed by several later compressional phases (Carvajal-Torres et al., 2022; Cooper et al., 1995; Espitia et al., 2022; Jiménez et al., 2012; Mora et al., 2010, 2020; Rosero et al., 2022) that may have been responsible for the development of an open and interconnected fracture network, which could have enhanced the flow and accumulation capacity.

In this contribution, we present a multi-scale structural analysis, including the identification of topographic lineaments, fracture analysis, and petrography, to investigate the structural evolution and evaluate the main factors controlling the fracture network properties. Additionally, low-temperature thermochronology, such as zircon fission-track, apatite fission-track, zircon U–Th/He, and apatite U–Th/He was used to constrain major deformational events. We aim to understand the plausible relations of fractures with the thermal and exhumation history of Jurassic igneous rocks within the damage zone of the regional Agrado-Betania Fault System, which thrusts the Jurassic basement against the Cretaceous-Cenozoic sedimentary rocks of the Upper Magdalena Valley Basin (Espitia et al., 2022; Jiménez et al., 2012; Rosero et al., 2022; Sarmiento and Rangel, 2004). These basement exposures could act as an outcrop analog for the UMVB because they share similar rock types and structural settings with subsurface system (Ukar et al., 2019).

Exposures of Jurassic igneous rocks in this polyphasic fault present an excellent opportunity to compare the effect of thrust fault deformation on contrasting magmatic lithologies. We highlight the importance of the diagenetic history of the volcaniclastic sequences and that their complex burial history, which results in the homogenization of the mechanical strength of different lithologies. Consequently, these lithologies exhibit a uniform response to subsequent brittle deformation. This contribution addresses a notable scientific gap concerning fractured basement reservoirs in volcanic settings with complex diagenetic histories.

2. Geological framework

2.1. Tectonic setting

The Cretaceous to recent uplift and sedimentation history of the Colombian Andes have been related to the interactions between the Nazca and Caribbean plates with the northwestern margin of the South American plate (Montes et al., 2019; Parra et al., 2012; Restrepo-Moreno et al., 2009; Siravo et al., 2019; Zapata et al., 2020; Villagómez and Spikings, 2013; Mora et al., 2020; Horton et al., 2020). As a result of the interactions, this orogen now includes the Western, Central, and Eastern Cordilleras, which are separated by the Cauca and Magdalena intermountain valleys (Fig. 1).

From the west, the Nazca Plate subducts obliquely underneath South America at a rate around 53–58 mm/yr, triggering right lateral transpressive movements in the overriding plate (Kellogg and Vega, 1995; Mora-Páez et al., 2019; Taboada et al., 2000; Trenkamp et al., 2002). The current convergence suggest a NE-SW direction of the maximum horizontal stress in this area (Mora-Páez et al., 2019), with shortening perpendicular to the margin and a northeast displacement with respect to the South American Plate at a rate 8.6 mm/year (Mora-Páez et al., 2019).

The Upper Magdalena Valley Basin is located between the southern segments of the Central and Eastern Cordilleras; this basin is divided into the Girardot and Neiva sub-basins by the SSW-NNE Natagaima-Patá structural high (Fig. 1; Beltrán and Gallo, 1968; Ramon and Rosero, 2006; Sarmiento and Rangel, 2004). The UMVB includes a protracted sedimentary history that began in the Cretaceous as part of a retroarc extensional basin that transitioned into a foreland basin during the Late Cretaceous-Paleogene due to the uplift of the Central Cordillera (Carvajal-Torres et al., 2022). Finally, the UMVB turned into a hinterland basin during the late Miocene, when the uplift of the southern Eastern Cordillera separated it from the Llanos and Putumayo basins (Bayona et al., 2008; Carvajal-Torres et al., 2022; Cooper et al., 1995; Mora et al., 2006, 2013; Pérez-Consuegra et al., 2021; Reyes-Harker et al., 2015; Zapata et al., 2023).

The structural evolution of the UMVB has been controlled by contractional events between the Late Cretaceous and Miocene, which have been responsible for deformation along several NNE-SSW regional thrust faults, which include the reactivation of the structures formed during an older Jurassic to Early Cretaceous extensional event (Fig. 1; Butler and Schamel, 1988; Espitia et al., 2022; Guerrero et al., 2021; Jaimes and de Freitas, 2006; Jiménez et al., 2012; Mora et al., 2010; Ramon and Rosero, 2006; Rosero et al., 2022; Villamizar-Escalante et al., 2021). The western and eastern boundaries of the basin have experienced thick-skinned deformation, through the La Plata-Chusma and the Algeciras fault systems (Fig. 1; Butler and Schamel, 1988; Saeid et al., 2017; Velandia et al., 2005). In contrast, combined thick and thin-skin deformation has been the dominant deformation style in the inner part of the UMVB, as observed along the Agrado-Betania and San Jacinto fault systems (Fig. 1b; Espitia et al., 2022; Jiménez et al., 2012). La Plata-Chusma fault system represents the limit between the eastern flank of the Central Cordillera and the basin. The contractional

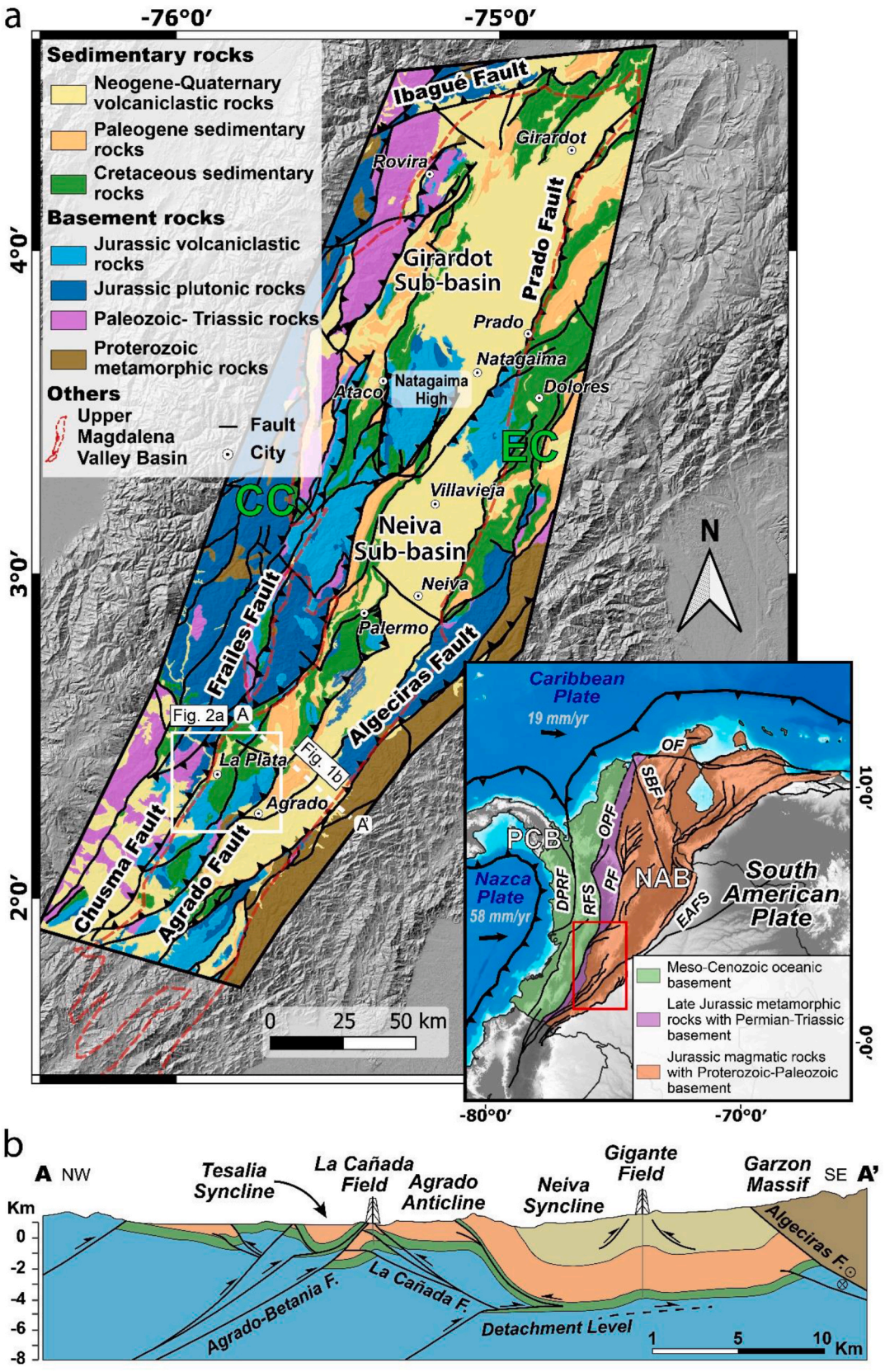

Fig. 1. Geological map showing regional thrust faults throughout the Upper Magdalena Valley Basin, modified after Gómez and Montes (2020). White box encloses the area in Fig. 2a; white dashed line represents the location of the A–A′ cross section shown in Fig. 1b. The inset map illustrates the current tectonic configuration of the Northern Colombian Andes; red box depicts the study area; vector motions, relative to stable South America, were taken from Mora-Páez et al. (2019). CC: Central Cordillera; EC: Eastern Cordillera; NAB: North Andean Block; PCB: Panamá-Chocó Block; DPRF: Dabeiba-Pueblo Rico Fault; RFS: Romeral Fault System; PF: Palestina Fault; OPF: Otú-Pericos Fault; SBF: Santa Marta-Bucaramanga Fault; OF: Oca Fault; EAFS: Eastern Frontal Fault System.

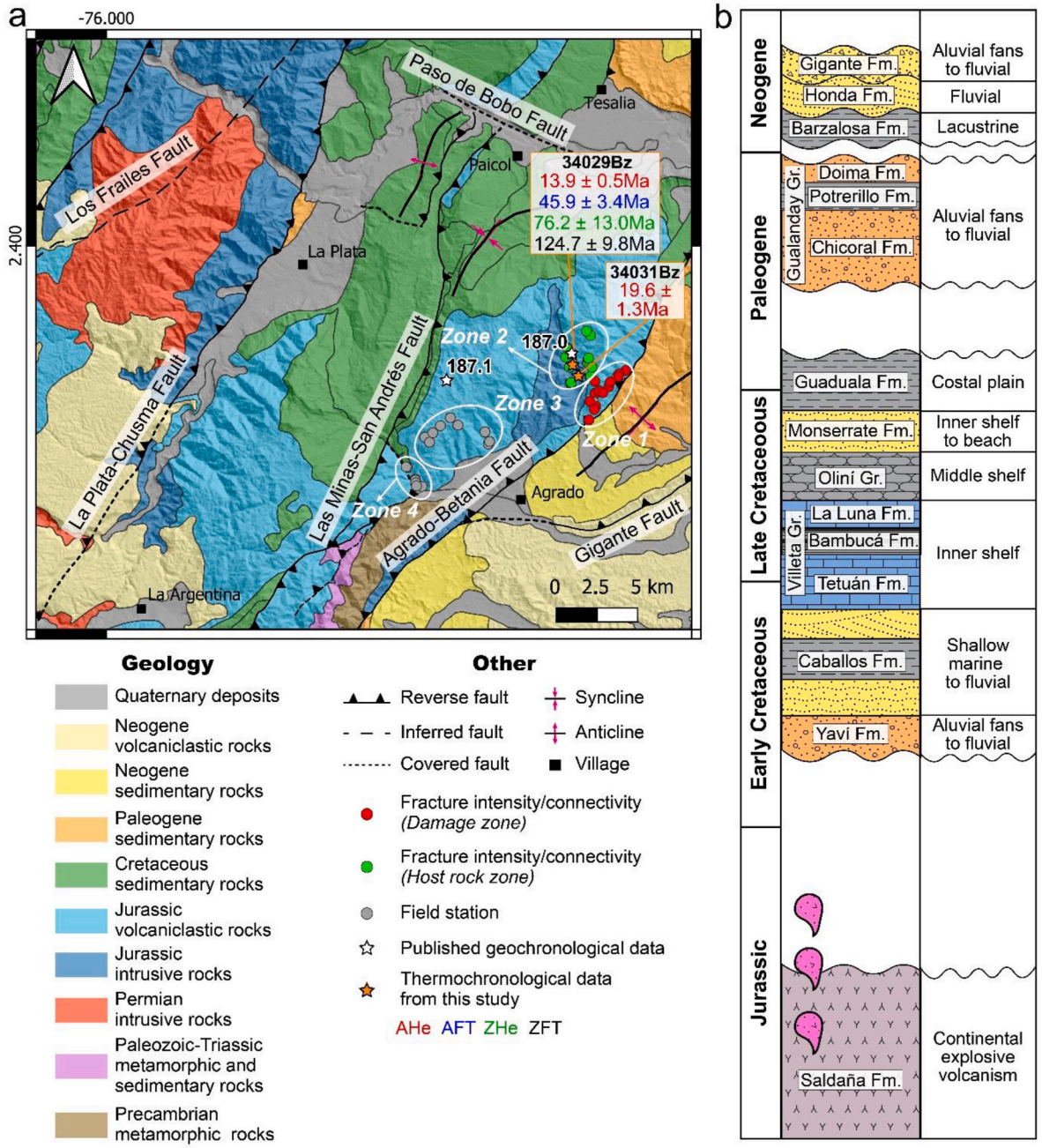

Fig. 2. a) Geological map of the study area (see Fig. 1 for location) showing the NNE-SSW striking Agrado-Betania fault system. The map was modified after Gómez and Montes (2020). Red and green dots are the field stations located in the damage zone and host rock zone of the Agrado-Betania fault respectively. White ellipses represent the four study zones of fracture orientations. Orange stars represent the location of the two thermochronological samples from the Astillero Pluton modeled in this study. White stars represent the location of the published geochronological data after (Rodríguez et al., 2016, 2018); b) Generalized stratigraphic section showing the main sedimentary units of the Upper Magdalena Valley Basin. Modified after Roncancio and Martínez (2011) and Sarmiento and Rangel (2004).

deformation migrated from La Plata-Chusma fault to the east of the basin through low-angle thrust faults (i.e., Dina and Palogrande Thrusts; de Thrusts; Butler and Schamel, 1988). These faults formed an eastward verging imbricate thrust belt including shallowly dipping basement-cored ramp anticlines (i.e., La Hocha Anticline and Upar High, Butler and Schamel, 1988; Jiménez et al., 2012).

Eastward dipping backthrusts (i.e., El Vergel Fault, La Cañada Fault) were developed associated with the ongoing contractional deformation related to the Mio-Pliocene uplift of the Eastern Cordillera (Anderson et al., 2016; Butler and Schamel, 1988).

The Agrado-Betania fault is a thrust fault striking NE-SW with a fault plane that dips steeply (~50–60°) to the west (Figs. 1 and 2; Butler and Schamel, 1988; Espitia et al., 2022; Jiménez et al., 2012). Seismic interpretation suggests that the deformation of this fault is associated with a fault throw of at least 4 km (Espitia et al., 2022). Volcanic rocks of the Jurassic Saldaña Formation and the Astillero Pluton are thrusted against the Miocene Gigante Formation by the Agrado-Betania fault, recording the latest-phase of deformation in the basin (Fig. 1b and 2a; Gómez and Montes, 2020).

Despite several studies focused on understanding the style and timing of the deformation on the UMVB, with the recognizing of an inversion history that occurred in several phases from the Eocene to the present day (Anderson et al., 2016; Butler and Schamel, 1988; Espitia et al., 2022; Jiménez et al., 2012; Mora et al., 2010; Saeid et al., 2017;

Villamizar-Escalante et al., 2021), the role of the basement in the structuration and the timing of deformation events have not been fully understood.

2.2. Petroleum system

The UMVB is one of the most prolific basins in Colombia, with significant oil and gas accumulations discovered since 1951 (Roncancio and Martínez, 2011). It encompasses over 30 oil and gas fields, with an annual production of approximately 18 million hydrocarbon barrels. The exploration efforts in these hydrocarbon accumulations have resulted in the discovery of 630 million barrels of oil and 123 billion cubic feet of gas across 38 fields (Roncancio and Martínez, 2011; Sarmiento and Rangel, 2004).

The Villeta Group encompasses the main hydrocarbon source rocks of the UMVB; this sedimentary succession was deposited during a maximum marine flooding event in the Cenomanian (Fig. 2b; Sarmiento-Rojas et al., 2006; Sarmiento and Rangel, 2004). Source rocks consist of shales and limestones deposited in an anoxic environment, with an average of Total Organic Carbon (TOC) ranging from 1% to 4% (Sarmiento and Rangel, 2004). The main reservoir rocks in the UMVB are deltaic quartz-arenites, which were formed during Aptian-Albian stages (i.e., Caballos Formation; Etayo-Serna and Carrillo, 1996, Fig. 2b) and Maastrichtian stage (i.e., Monserrate Formation; Sarmiento and Rangel, 2004: Fig. 2b). Other minor reservoirs include fluvial to alluvial fan environments of Eocene to Miocene ages, associated with the Chicoral, Doima, and Honda formations (Fig. 2b). The primary seal rocks in the basin are composed of muddy Cenozoic fluvial and lacustrine sedimentary rocks within the San Francisco, Potrerillos, Barzalosa, and Honda formations (Ramon and Rosero, 2006; Sarmiento and Rangel, 2004).

The deformation history of the UMVB has resulted in the structural juxtaposition of Jurassic plutonic and volcanic rocks on top of the Meso-Cenozoic hydrocarbon source rocks (i.e., Villeta Group) and reservoir rocks (i.e., Caballos and Monserrate Formations) (Ramon and Rosero, 2006; Sarmiento and Rangel, 2004). Many wells producing conventional hydrocarbons are located in the footwall of the Agrado-Betania and San Jacinto faults, where the Jurassic basement is in contact with the producing rocks (Fig. 1b–Espitia et al., 2022; Jiménez et al., 2012). Drilled wells have proven that the igneous Jurassic rocks represent the underlying pre-Cretaceous basement in most of the UMVB (de Freitas, 2000).

Basin subsidence and sedimentation was the main mechanism responsible for organic maturation in depocenters where sediment thickness reached a maximum before any tectonic burial. Additionally, organic maturation occurred in some pods due to tectonic stacking of thrust sheets in the western part of the basin, resulting from contractional events between the Eocene and Miocene periods (Sarmiento and Rangel, 2004). Stratigraphic traps were developed during Meso-Cenozoic sedimentation, while structural traps primarily formed during the Mio-Pliocene deformation. Furthermore, hydrocarbon migration occurred from the Miocene to the present day in most of the basin (Ramon and Rosero, 2006; Sarmiento and Rangel, 2004).

2.3. Jurassic igneous rocks

Jurassic volcanic and plutonic rocks are widely distributed in the Northern Andes of Ecuador and Colombia. These rocks units are exposed along discontinuous and elongated NNE-SSW bodies in the Central and Eastern Cordilleras of Colombia, as well as in the Upper and Middle Magdalena Valleys (Bayona et al., 2006, 2010, 2020; Bustamante et al., 2010, 2017; Leal-Mejía et al., 2019; Rodríguez–García et al., 2020; Spikings et al., 2015). They include plutonic rocks from the Ibagué Batholith, the Paez Massif, the Algeciras Massif, and the Astillero Pluton, as well as the volcaniclastic Saldaña Formation (Fig. 1; Gómez and Montes, 2020). Within the Neiva Sub-basin, in the southern sector of the UMVB, several well-preserved outcrops of Jurassic igneous rocks are present around its western and eastern boundaries.

The Jurassic plutonic rocks throughout the UMVB are grouped into a mafic-intermediate quartzmonzonite-quartzdiorite series and the most evolved ones are grouped in the granodiorite-syenogranite series (Rodríguez et al., 2018). Geochemical and geochronological constraints suggest that these rocks are related to a long-lived magmatic arc on a continental margin that was active between 195 Ma and 153 Ma (Bayona et al., 2020; Bustamante et al., 2010, 2016; Restrepo et al., 2021; Rodríguez et al., 2018, 2020).

Volcaniclastic and plutonic rocks related to the Saldaña Formation are the basement of the UMVB (Fig. 1). The Saldaña Formation overlays Late Triassic calcareous rocks from the Payandé Formation in the northern part of the basin (Girardot Sub-basin); however, in the Neiva sub-basin this relationship is not clear, therefore crystalline rocks are referred to as pre-Cretaceous basement (Espitia et al., 2022). The Barremian fluvial Yaví Formation and the deltaic Albian-Aptian Caballos Formation overlay the Jurassic volcaniclastic basement through a well-defined angular unconformity (Fig. 2a; Cediel et al., 1980). The Saldaña Formation has been separated into the lower Chicalá and upper Prado members, which record the transition from shallow marine depositional systems with minor volcanic contribution to fluvial continental environments dominated by explosive volcanic activity (Bayona et al., 1994; Mojica and Llinás, 1984). The fossiliferous record of the Chicalá Member indicates a Rhaetian (Late Triassic) age for its sedimentation (Mojica and Llinás, 1984). Petrography, geochemistry, and geochronology data from the Prado Member in the UMVB suggest that these rocks were also part of the continental magmatic arc with crystallization ages between 189 Ma and 168 Ma (Bayona et al., 1994; Rodríguez et al., 2016).

This Jurassic magmatic record has been related to a transtensional tectonic setting, being also affected by northward strike-slip displacement between the Late Jurassic and the Early Cretaceous as a result of the oblique convergence between the Farallon oceanic plate and northwestern South America (Bayona et al., 2006, 2010, 2020; Bustamante et al., 2010).

3. Methodology

We conducted a multiscale analysis in the SW portion of the UMVB, near the Agrado town (Fig. 2a), where the igneous Jurassic basement (i.e., Saldaña Formation and Astillero Pluton) is well exposed in the hanging-wall of the Agrado-Betania fault system. Because we analyzed an outcrop analog, the lack of subsurface data is a limitation for predicting how the fracture properties and reservoir quality can change with depth.

We mapped macroscale topographic lineaments using satellite data, mesoscale outcrop analysis using scanlines and circular windows, and a microscale study using thin sections of rock samples. Also, these methods were integrated with low-temperature thermochronological and petrophysical data to assess the structural evolution and reservoir quality of the igneous rocks, that are exposed in the hanging-wall of the Agrado-Betania fault.

3.1. Topographic lineament analysis

The development of linear features on the surface such as drainage, crests, and valleys have been associated with fault and fracture zones (Wise et al., 1985). Several workers have utilized topographic lineament mapping, through remote sensing, to characterize regional scale, sub-parallel linear topographic features, referred to as “lineaments” (Cianfarra and Salvini, 2015; Wise et al., 1985 and references therein).

The regional topographic lineament analysis was carried out following the methodology proposed by Wise et al. (1985) and implemented by Celestino et al. (2020). A Digital Elevation Model was freely downloaded from the Alos-1 Palsar satellite through the website https://asf.alaska.edu, which provides 12.5 m of spatial resolution per

pixel. Crests and valleys were discriminated through an interactive shadowing technique in different orientations of light incidence (Az0°, Az45°, Az270°, and Az315°) using the QGIS 3.18 software on a Digital Elevation Model (DEM) (Fig. 3a). We have selected the southwestern segment of the Upper Magdalena Valley Basin (Neiva Sub-basin) and the Central Cordillera, where La Plata-Chusma and Agrado-Betania fault systems are well exposed (Fig. 2a) to perform the lineament analysis (Fig. 3a). As a result, the lineaments were manually drawn over an area of ~1452 Km^2.

Lineament orientations and lengths were calculated through the NetworkGT plugin in QGIS (Nyberg et al., 2018), and plotted on rose diagrams using the Stereonet software (Cardozo and Allmendinger, 2013). Additionally, 2D lineament intensity was calculated following the circular window scanning method with 100 m grid cells and a sampling window with a 900 m radius (Cawood et al., 2023; Mauldon et al., 2001).

3.2. Field observations and petrography

Lithological descriptions include composition, classification, grain size, and weathering. The description of ignimbrites was conducted following the non-genetic lithofacies scheme from Branney and Kokelaar (2002), sedimentary lithologies were classified after Folk (1980), and igneous rocks were classified according to Le Maitre (2002).

The petrographic analysis followed the conventional methodology (Suttner et al., 1981), encompassing the identification of grain types, characteristic textures, and interstitial materials such as cement, matrix, and pores. The petrographic description of ignimbrites was conducted by describing matrix, vesicles, crystals, shards, and lithic fragments, and their compositional and textural characteristics (McPhie et al., 1993).

3.3. Outcrop fracture analysis

3.3.1. Fracture intensity and connectivity

The outcrop fracture study included the measurement of the fracture orientations in forty-seven field stations exposed throughout a west-east cross-section perpendicular to the Agrado-Betania fault (Fig. 2a). Topology, fracture intensity analysis, porosity, and permeability calculations were carried out in twenty-one stations.

The fracture properties, such as aperture, spacing, fill, and fracture relationships, were also described (Peacock et al., 2018). Fracture intensity and topology was evaluated following the scan line (Priest and

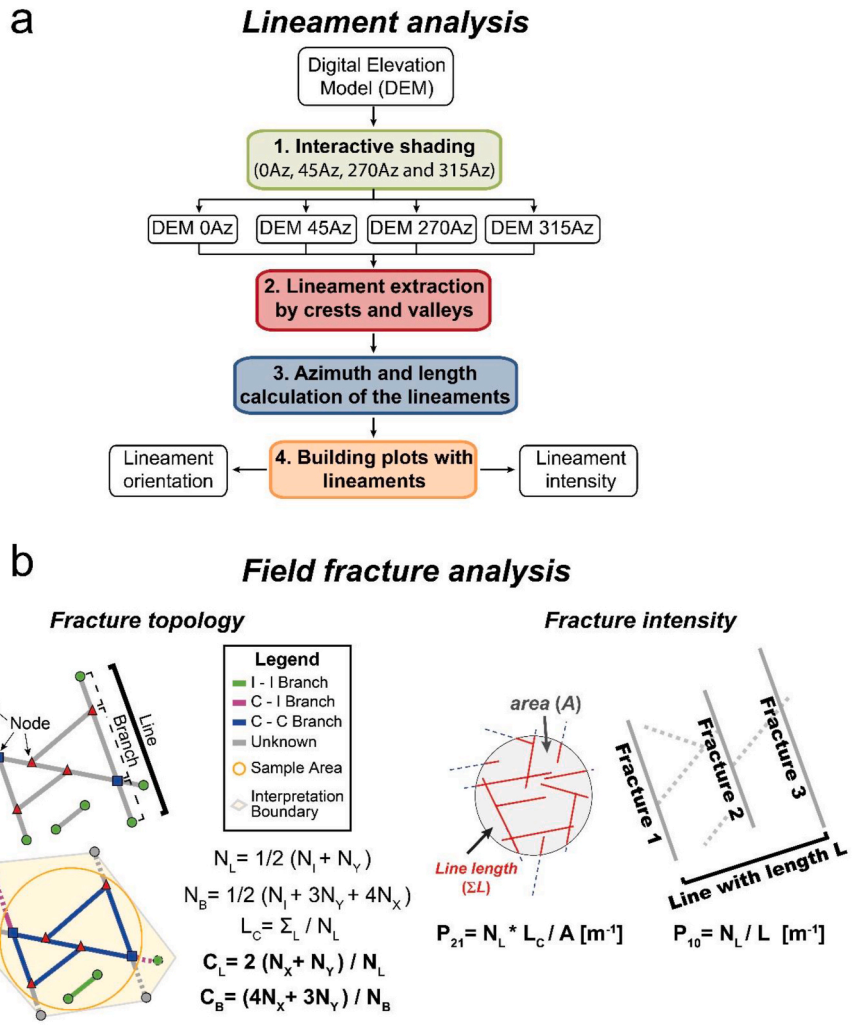

Fig. 3. a) Flowchart illustrating the sequence of steps conducted during the analysis of topographic lineaments extracted from the digital elevation model. Modified from Celestino et al. (2020); b) Explanation of the fracture network configuration based on lines, nodes, and branches when evaluated in a two-dimensional context after Nyberg et al. (2018). The nodes within the fracture network are categorized as either isolated nodes (I) or connecting nodes (Y or X). Also, the branches are categorized as either isolated branches (I–I), singly connecting branches (C–I) or doubly connected branches (C–C). This classification is applied within a defined sample area and interpretation boundary. C_B: average connections per branch; C_L: average connections per line; P_{10}: 1-D frequency; P_{10}: fracture intensity (areal intensity); N_I: number of I nodes; N_X: number of X nodes; N_Y: number of Y nodes; L_C: characteristic length; N_L: total lines; N_B: total branches.

Hudson, 1981), and the circular scanning window methodologies (Mauldon et al., 2001; Rohrbaugh et al., 2002; Sanderson and Nixon, 2015, 2018; Watkins et al., 2015, Tables 1 and 2).

Sanderson and Nixon (2015) proposed a relationship between connectivity and fracture intensity, using the tips of the fracture segments, called nodes (Fig. 3b). Isolated nodes ("I type") are connected only by one branch, abutting nodes ("Y type") are connected by three branches, and crossed nodes ("X type") are connected by four branches (Fig. 3b).

The linear frequency, also known as P10 intensity by some authors, was determined by counting the number of fractures per unit length (P10 = # fractures/meter). Since fracture-size distributions typically follow power-law or exponential scaling, associating a size descriptor (aperture) with the P_{10} intensity enhances the usefulness of this parameter (Ortega et al., 2006). This adjustment is crucial because a set of fractures has a more significant impact when they are larger (wider) compared to the same number of smaller (narrower) fractures. Therefore, we adopted the scale-independent approach to fracture intensity proposed by Ortega et al. (2006). This approach involves calculating a cumulative-frequency fracture-size distribution, which provides a comprehensive measure of fracture intensity that explicitly considers fracture size allowing comparisons at different locations and observation scales. To facilitate comparisons among all datasets, we standardized fracture intensities using a consistent fracture-aperture threshold of 0.2 mm (Ortega et al., 2006). Fracture aperture was measured using a logarithmically graduated comparator.

The areal fracture intensity, known as P_{21}, refers to the total length of fractures in meters per unit area (P_{21} = total length of fracture (m)/total area (m^2)). Areal intensity is estimated within a circular area with different defined radius, which must encompass more than 30 nodes. In this area the number of "I", "Y" and "X" nodes must be counted to calculate the number of lines (N_L) and the average length of lines (L_C) (see equation in Fig. 3b–Sanderson and Nixon, 2015). We were not able to measure the P32 fracture intensity value because most of the outcrops were exposed in only 2 dimensions.

Branches can be classified as isolated ("II types"), partially connected ("IC type"), and totally connected ("CC type"). A high amount of "X" and "Y" nodes indicates high fracture connectivity. Therefore, following the equation in Fig. 3b, the average connection per branch index (C_B) is used to assess the connectivity of a fracture system. This index can be calculated in terms of the sum of "X" and "Y" nodes divided by the number of branches (N_B) in the circular scanning area. Hence, values of C_B higher than 1.5 suggest a highly connected network of fractures (Sanderson and Nixon, 2018). Similarly, we computed the average connection per line index (C_L) using the proportion of "X" and "Y" nodes (Sanderson and Nixon, 2018).

Forstner and Laubach (2022) have recently proposed a novel methodology in which connectivity descriptions should include accurate measurements of fracture properties by employing "contingent" nodes (C nodes) that consider both scale and diagenesis. The contingent nodes are useful when complex interactions between fracture segments exist, for instance, where en-echelon segments overlap (Forstner and Laubach, 2022). Hence, their intersection relations are ambiguous, leading to uncertainties in defining connectivity and length (Forstner and Laubach, 2022). However, as our study did not identify a significant number of overlapping fractures or an abundance of mineral-filled fractures, we decided not to consider contingent nodes. Instead, we followed the methodology proposed by Sanderson and Nixon (2018) since it remains suitable and valuable for our specific study.

3.3.2. Evaluation of the fault damage zone

Fracture intensity was conducted at twenty-three stations in order to estimate the width of the fault damage zone. This analysis was carried out in different lithologies to explore the possible control of lithology in fracture intensity by comparing bar diagrams per lithology in both damage zone and host rock (Fig. 6d and e).

Bar diagrams of P_{10} intensity versus cumulative frequency were plotted to assess the behavior of the cumulative frequency curve as a function of distance from the fault core (Choi et al., 2016). The width of the damage zone was determined by identifying an abrupt reduction in the slope of the cumulative frequency curve, which marks a decrease of fracture intensity and defines the boundary of the damage zone (Choi et al., 2016).

3.4. Petrophysics

Twenty-two core plug samples from different lithofacies of the Saldaña Formation and the Astillero Pluton distributed among seventeen field stations, were collected within the hanging-wall of the Agrado-Betania fault to calculate matrix porosity and permeability. In five stations, core plugs were drilled in two orientations perpendicular and parallel with respect to a fracture plane, to evaluate fluid flow anisotropy. Fracture porosity and permeability were estimated, in the same outcrops where the matrix plugs were taken, by using equations proposed by Tiab and Donaldson (2015) and Marrett (1996). These petrophysical properties were computed firstly on individual fractures, using fracture properties such as intensity, aperture, spacing, and average fracture length (Table S3). Then, matrix values were added to compute the total porosity and permeability for each outcrop.

3.4.1. Matrix porosity

The measurements of porosity of the core plugs were carried out based on Boyle's Law of gas expansion in the Petrorocas S.A.S Laboratory, Medellín, Colombia. Then, grain volume (V_{grain}) was obtained from a dry sample, where helium is injected and expanded into a chamber containing the core plugs (Tiab and Donaldson, 2015). The pressure needs to be recorded in each step. Pore volume (V_{pore}) was calculated through the difference between bulk volume and grain volume (V_{grain}). Finally, porosity (φ) was computed using these values.

3.4.2. Matrix permeability

A gas permeameter was used to estimate the permeability of the core samples, in which the pressure difference was measured until a steady state was reached. This test was conducted in a 100% saturated sample with a brine with a defined concentration of salts. The bulk permeability was determined following Darcy's law, which relates the fluid flow across a transversal area and a determined length (Tiab and Donaldson, 2015).

3.4.3. Fracture porosity and permeability

Petrophysic analysis also included fracture porosity and permeability calculations, which were computed in terms of fracture attributes such as intensity, aperture, and average fracture height following the methodology for petrophysical properties estimations of naturally fractured rocks proposed by Tiab and Donaldson (2015). Given that fracture aperture populations follow power-law or negative exponential distributions, we also performed the calculations of fracture porosity and permeability following the equations proposed by Marrett (1996), to compare the results obtained by both methodologies.

The porosity of a fracture network was calculated with Equation (3.1) after Tiab and Donaldson (2015).

$$\varphi_{fractures} = (P_{10} * a_{av}) * 100 \tag{3.1}$$

where P_{10} = fracture intensity (# fractures/m) and a_{av} = mean aperture (m). Furthermore, the aggregate fracture porosity was calculated with Equation (3.2) after Marrett (1996):

$$\varphi_T = \sum \frac{a}{R_T} * 100 \tag{3.2}$$

where a = aperture of each fracture (cm) and R_T = sampling line. Before estimating the permeability of a fracture set, single fracture permeability must be calculated following Equation (3.3) defined by Tiab and

Donaldson (2015):

$$K_{fracture} = 8.444 * 10^{6} * (a_{av})^{2} \quad (3.3)$$

where $K_{fracture}$ = permeability of a single fracture (Da), and a_{av} = mean aperture (cm). Then, effective permeability, which is computed in terms of fracture and matrix permeability, can be estimated using Equation (3.4), suggested by Tiab and Donaldson (2015):

$$K_{eff} = \frac{(n_f * a_{av} * H_{av}) * K_{fracture}}{A} + \left(1 - \frac{(n_f * a_{av} * H_{av}) * K_{fracture}}{A}\right) * K_m \quad (3.4)$$

where K_{eff} = effective permeability (Da), K_m = matrix permeability (Da), $K_{fracture}$ = permeability of a single fracture (Da), H_{av} = average height of fractures (cm), n_f = number of fractures per area, A = circular window area (cm^2), and a_{av} = mean aperture (cm).

Finally, the aggregate fracture permeability was calculated with Equation (3.5) after Marrett (1996):

$$K_T = \sum \frac{a^3}{12R_T} \quad (3.5)$$

where a = aperture of each fracture (cm) and R_T = sampling line. Additionally, the effective permeability and porosity were calculated with the minimum aperture from each outcrop. The results were then reduced by 70% to approximate the values to well conditions and to enable the comparison with other data following the results of Rashid et al. (2023), who found that fracture permeability was reduced around four orders of magnitude from 0 PSI to 4000 PSI.

3.5. Low-temperature thermochronology and inverse thermal history modeling

Thermochronology is based on the quantification of decay products following the closure of an isotopic system (e.g., Harrison, 2005; Reiners, 2005). In the zircon (ZFT) and apatite (AFT) fission-track methods, lattice damage (tracks) resulting from the spontaneous fission of U^{238} are quantified (e.g., Malusà and Fitzgerald, 2019). These tracks can be annealed at temperatures ranging from approximately 60 °C–120 °C for apatite (Green et al., 1986) and 180–300 °C for zircon (Bernet, 2009), defining the apatite and zircon partial annealing zones, respectively. In apatites, the distribution of track lengths can be related to the sample trajectory through the partial annealing zone (Green et al., 1985). The analyses were carried out at the Low-Temperature Thermochronology Laboratory (LabTer) of São Paulo University. Detailed procedures are presented in Zapata et al. (2020) and Patiño et al. (2019).

The apatite (AHe) and zircon (ZHe) helium methods consist of measuring the helium accumulated in the crystal lattice as result of the decay of uranium (^{238}U and ^{235}U), thorium (^{232}Th), and samarium (^{147}Sm) (only in apatites). The capacity of zircon and apatite to retain helium is highly influenced by grain size, cooling rates and the amount of radiation damage, which is proportional to the amount of parent isotopes (effective uranium; eU = u + 0.235*Th). Under cooling rates of ~10 °C/Ma, apatites can partially retain helium within a temperature range from 40 to 90 °C, while typical zircons can retain helium within a range of 140–220 °C (Flowers et al., 2009; Guenthner et al., 2013; Shuster et al., 2006). Only reproducible ages (SD < 20% of the mean age) and single-grain aliquots that exhibit size or eU intra-sample trend susceptible of modeling were included in the model (Brown et al., 2013; Flowers et al., 2009; Guenthner et al., 2013). The grain degassing was conducted at the Alphachron laboratory at Potsdam University, while the measurement of U, Th, and Sm concentrations was carried out at the German Research Center of Geoscience (GFZ). Detailed procedures are presented in Zapata et al. (2019a).

The most likely thermal history was obtained from the data using the QTQt software (Gallagher, 2012). The AHe models employed the kinetic model proposed by Flowers et al. (2009), the Guenthner et al. (2013) model was used for ZHe data, and the one of Ketcham et al. (2007) for AFT data. The initial 250,000 iterations were discarded (burn-in stage), and the subsequent 250,000 iterations were used to calculate the posterior probability. Two geological constraints were incorporated into the model to account for the pluton's crystallization age and the observed unconformity between the basement and Cretaceous strata (Fig. 2a). This relatively large unconformity constraint was established between 140 Ma and 100 Ma due to the lack of accurate depositional ages of the Caballos Formation in our study area. The model was allowed to generate solutions within the time range of 0 Ma to 200 Ma and the temperature range of 0 °C–200 °C.

4. Results

4.1. Topographic lineament analysis

Differences in lineament orientations can be observed between each shadowing direction, with Az45° direction showing predominantly a NW-SE orientation, while the Az315° being characterized by a NE-SW direction (Fig. 4a). However, the orientations of crests and valleys exhibit similar distributions. We therefore plotted crests and valleys topographic lineaments on a single rose diagram, including all shadowing directions (Fig. 4b). The integrated rose diagram reveals that lineaments are mainly distributed with three preferred orientations: NE-SW, N–S, and NW-SE, with a secondary E-W orientation (Fig. 4b). The topographic lineaments orientations follow the fault strikes in the study area, as can be observed in the NE-SW striking faults (i.e., Los Frailes, La Plata-Chusma, and Agrado-Betania faults), as well as the NW-SE striking faults (i.e., El Paso de Bobo fault, Fig. 2a, 4b and 4c), which are exposed in the published fault maps. The fault-lineament correlation was also observed in some outcrops, where the strike of faults mostly follows the lineament orientations. For instance, the fracture orientation measurements carried out in zones 3 and 4 showed NW-SE striking faults (Fig. 4d).

The 2D lineament intensity reaches higher values in the westernmost part of the study area (~0.02 m/m^2), where Permian and Jurassic plutonic rocks are extensively exposed (i.e., La Plata granite and Paez Massif). In contrast, the eastern part, characterized by volcaniclastic rocks (i.e., Saldaña Formation), exhibits lower values (~0.002–0.016 m/m^2, Fig. 4c).

Crystalline rocks located near the regional faults exhibit higher lineament intensity compared to those farther away (Fig. 4). For instance, within the hanging-wall of the Agrado-Betania and La Plata-Chusma faults (Fig. 4c). However, in the case of the westernmost Los Frailes Fault and La Plata-Chusma Fault, there are no clear relationships between lineament intensity and proximity to the fault. High lineament intensity is also associated with NW lineament orientations (i.e., Agrado-Betania fault; Fig. 4c and d). We highlight the presence of these 'off-fault' areas with high lineament intensity, situated in the hanging wall of both La Plata-Chusma Fault and Los Frailes Fault, because they exhibit the highest intensities within our study region (Fig. 4c).

4.2. Field observations and petrography

The volcaniclastic record of the Saldaña Formation consists of a discontinuous section of ~2.5 km of stratigraphic thickness. The field observations show a monoclinal structure with the strata dipping 40° and dip azimuth orientation around ~320°. Furthermore, an angular unconformity with the Lower Cretaceous Caballos Formation was identified in the northwestern part of the Agrado-Betania hanging-wall (Fig. 2).

The stratigraphy of the Saldaña Formation in the hanging-wall of the Agrado-Betania fault is represented by thick beds (~1–2 m) of massive volcanic rocks, which are interbedded with a few beds of red, parallel

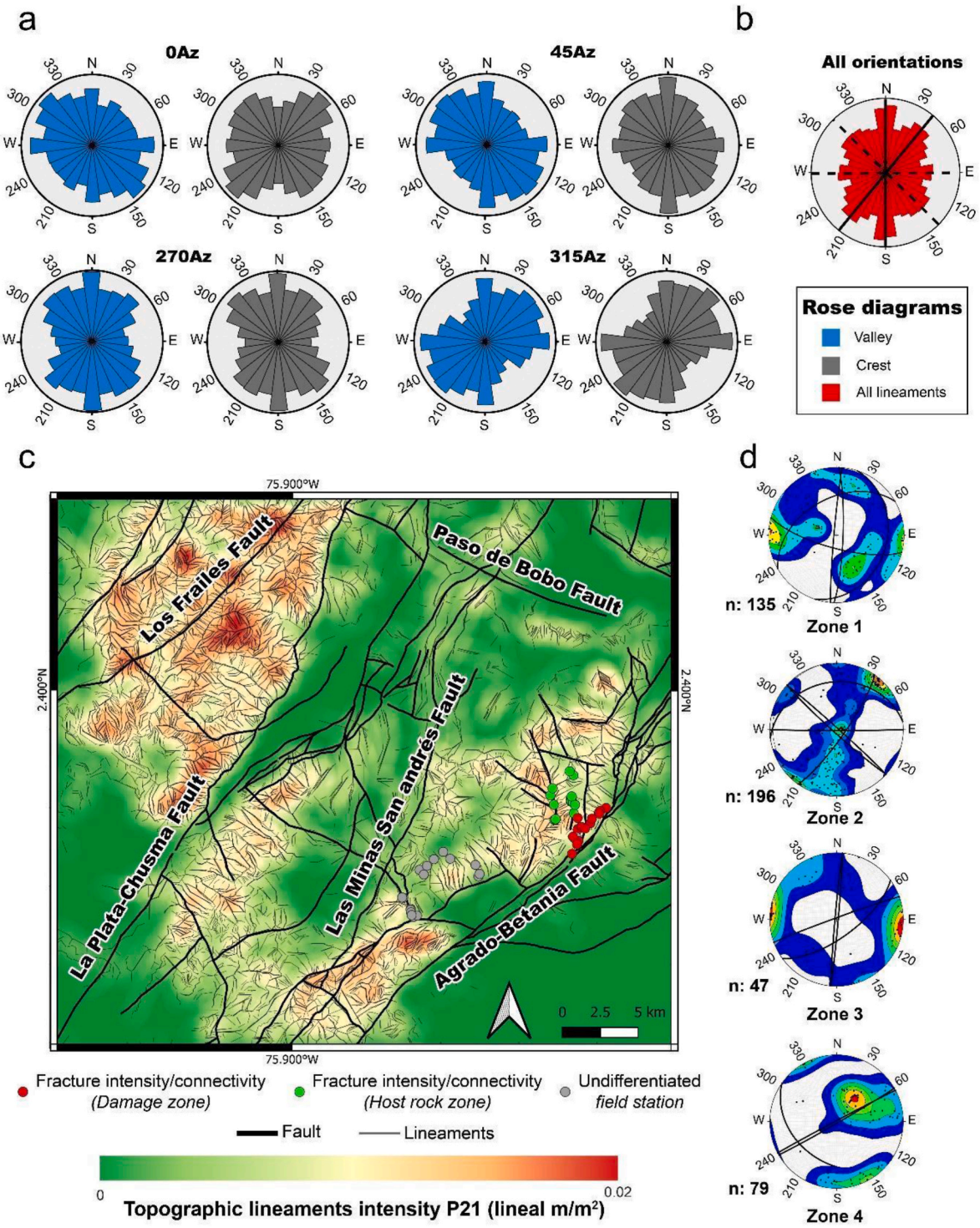

Fig. 4. a) Lineament orientations represented by rose diagrams in different illumination directions (0Az, 45Az, 270Az, and 315Az) separated by crests and valleys. Lineament orientation includes both basin and basement features; b) All lineament directions showing the four main orientations of structures in the study zone (NE, N–S, NW, and E-W); c) 2D lineament intensity calculated using the Line Density tool in QGIS 3.18 (Cawood et al., 2023). The Line Density tool of QGIS conducts the intensity estimation following the circular window scanning methodology proposed by Mauldon et al. (2001); d) Lower hemisphere stereographic projections of poles to fracture and fault planes, with some planes plotted as great circles to show dominant trends portraying the main fracture orientations of each selected zone. Zones are defined in Section 4.3.

laminated mudstones and gray chert. Also, there are some beds of massive tuffaceous sandstones and matrix-to-clast-supported conglomerates, interbedded with the volcanic rocks.

Volcanic lithologies include massive and poorly sorted volcanic breccias and lapilli tuffs with angular to subangular fragments of pink pumice, lithic fragments, and some crystals of alkali feldspar and plagioclase (Fig. 5). The most common lithologies in the Saldaña Formation are massive, well sorted, red to violet ash tuffs, which range from shard-rich to crystal-rich compositions with vitriclastic texture in the matrix, where the glassy shards are well preserved (Fig. 5e). Crystals of

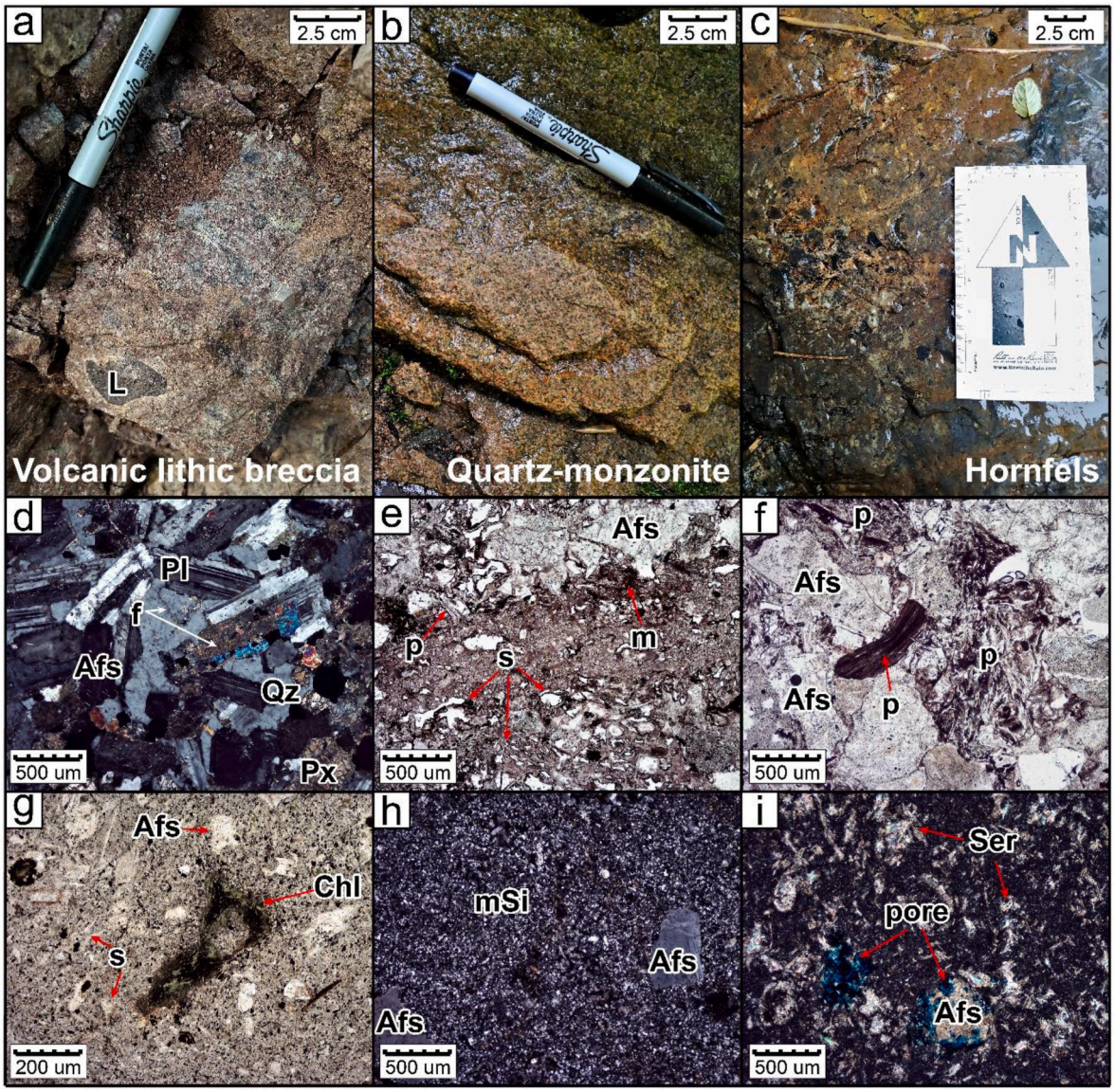

Fig. 5. Field and petrographic characteristics from Jurassic igneous rocks that are exposed in the hanging-wall of the Agrado-Betania fault. a) Volcanic lithic breccia; b) Quartz-monzonite from the Astillero Pluton; c) Hornfels after sedimentary breccia from the Saldaña Formation; d) Petrographic details of the quartz-monzodioritic facies from the Astillero Pluton showing some intragranular microfractures; e) Shard-rich ash tuff displaying vitriclastic texture and alkali feldspar crystals; f) Tuffaceous litho-arenite showing flexion of pumice fragments and pseudomatrix formation after juvenile fragments; g) Crystal-rich ash tuff with disseminated chlorite; h) Crystal-rich ash tuff displaying pervasive silicification and broken crystals of alkali feldspar; i) Crystal-rich ash tuff with disseminated chlorite and dissolution pores after feldspar crystals. L: lithic; Afs: alkali feldspar; Pl: plagioclase; Px: pyroxene; Qz: quartz; Chl: chlorite; Ser: sericite p: pumice fragment; m: matrix; s: shard glass; mSi: matrix with silicification.

alkali feldspar, plagioclase, and quartz are predominant components in most of the samples, whose composition ranges from quartz-latite to alkali feldspar trachyte. Overall, some volcaniclastic rocks exhibit incipient to intense eutaxitic fabric of deformed juvenile pyroclasts, which is appreciable both on outcrops and thin sections. Also, the flexion of juvenile fragments, development of pseudomatrix after pumice fragments, and sutured contact between framework grains are pieces of evidence of high compaction (Fig. 5f).

The Astillero Pluton intrudes the Saldaña Formation, generating thermal effects evidenced by the formation of hornfels and causing a pervasive silicification of these volcanics rocks (Fig. 5b, c, and 5d). This igneous body is composed of massive to porphyritic, gray to pinkish-colored quartz monzodiorites and quartz monzonites (Fig. 5b). These rocks predominantly consist of plagioclase, alkali feldspar, and quartz, with a lesser proportion of mafic minerals, including clinopyroxene, amphibole, and biotite. Intragranular microcracks are observed in the plagioclase (Fig. 5d).

Rocks in the Saldaña Formation display several diagenetic minerals and pervasive silicification. The most common product is silica, which is pervasively disseminated through volcanic rocks. Non-coherent volcanic rocks display felsitic and axiolitic textures. Furthermore, some samples exhibit a different mineral paragenesis as a result of devitrification, such as disseminated chlorite, sericite, silica, and epidote (Fig. 5g and h); while a few samples show vesicular features and dissolution pores that enhance the secondary porosity in volcanic rocks (Fig. 5i; see discussion).

4.3. Outcrop fracture analysis

4.3.1. Fracture characteristics and orientations

The Agrado-Betania fault thrusts Jurassic igneous rocks against Meso-Cenozoic sedimentary rocks from the UMVB (Fig. 2a). Fault

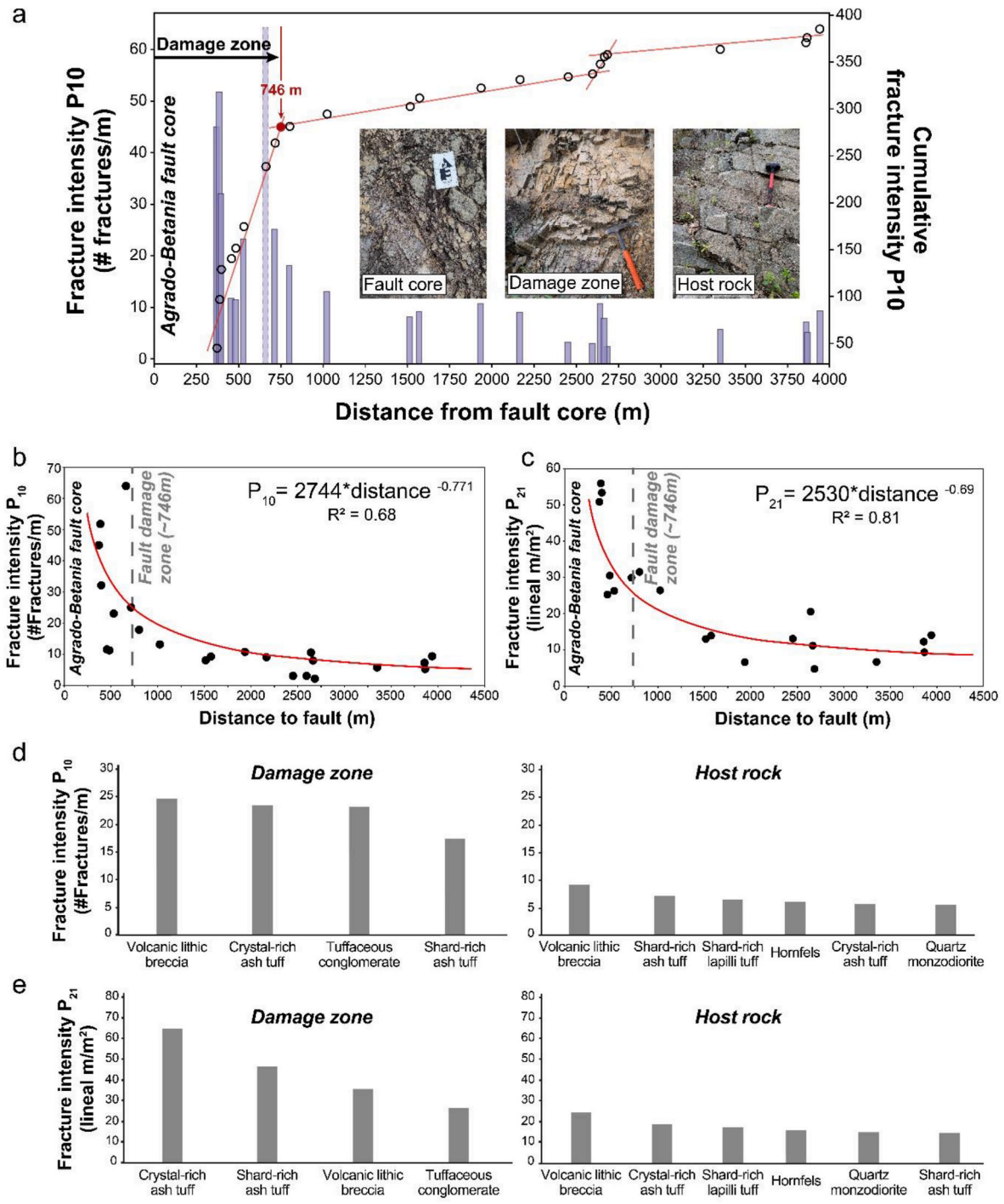

Fig. 6. Summary of fracture intensity analysis in the hanging-wall of the Agrado-Betania fault. a) Damage zone width calculation using the frequency of brittle structures and cumulative frequency following the methodology proposed by Choi et al. (2016). The zero in the X-axis represents the Agrado-Betania fault core. Y-axis represents frequency data and the cumulative frequency of brittle structures. Blue bars represent the P_{10} fracture intensity from each outcrop. Photographs display the characteristics of each fault architecture zone; b) Relationship between P_{10} fracture intensity and fault core distance resulting in a power-law distribution; c) Relationship between P_{21} fracture intensity and fault core distance resulting in a power-law distribution; d) P_{10} fracture intensity by lithology; e) P_{21} fracture intensity by lithology.

architecture, including the core, damage zone, and host rock, was identified (Fig. 6). Transverse faults and different lithologies are also exposed across the area.

We divided this fault into four zones to evaluate the changes in the fracture network along its hanging-wall (Fig. 2a). The results of fracture orientation and characterization are summarized in Table 1.

Conjugate open shear fractures, with slickensides developed in the fault planes, are the most common type in the area. However, extensional fractures with smooth planes are also observed. In the described field stations, it was not possible to achieve the differentiation between shear fractures and extensional fractures due to the quality of the outcrops. Mineralized slickensides were found in some outcrops. These are characterized by the presence of minerals such as plagioclase, quartz, and alkali feldspar in the fault damage zone, whereas in the vicinity of the fault core, sericite and chlorite were the most common minerals found along faults and fractures. Despite this mineralization,

Table 1
Summary of the main fracture sets characteristics in the outcrop analog within the hanging-wall of the Agrado-Betania fault. The detailed fracture orientation and aperture measurements are presented in Tables S1 and S2 respectively.

Fracture set	Main orientation (Dip/Dip azimuth)	Mineralization	Relative age relationships	Minimum aperture (mm)	Mean aperture (mm)	Maximum aperture (mm)
NNW-SSE	5-10/250-270	Open/Some of them with cataclasites and plagioclase slickensides through secondary fault planes	The youngest fracture set in the area (exhumation fractures), which is posterior to fractures sets NE-SW and N–S	0.095	0.731	5.000
NE-SW	50-80/315-330	Open/Some of them with feldspar slickensides through secondary fault planes	These two sets have an intermediate age and were probably developed together as a result of the Agrado-Betania faul evolution.	0.050	0.547	2.150
N–S	60-88/260-275	Open/Some of them with quartz		0.175	1.652	10.000
NW-SE	30-40/210-220	Epidote-Chlorite-Sericite	The oldest fractures set in the area. This fracture and fault orientation is probably related to NW-SE inherited structures in the basement. This set is prior to NE-SW, N–S, and NNW-SSE fractures set.	0.215	1.058	6.000

fractures are usually open. Some open fracture sets postdate the sericite and chlorite mineralization; however, there was also reactivation after mineralization through some pre-existing fault planes.

Zone 1 (Fig. 2a), which is located near the core of the Agrado-Betania fault, is characterized by two predominant fracture sets. One fracture set trends in a north-south direction, displaying a steep dip angle ranging from 45° to 80°, while the other one has a northeast-southwest trend with a dipping angle of ~60°–75° (Fig. 4d). Open shear fractures are the dominant type of discontinuities found in zone 1. Alkali feldspar and plagioclase slickensides that are recognized together with some ~10 cm width cataclasites indicate the presence of secondary faults with N–S and NNW-SSE orientations in the zone (Table 1 and Table S1).

Zone 2 includes the Saldaña Formation and the Astillero Pluton in a distal position with respect to the Agrado-Betania fault core (Fig. 2a). The Astillero Pluton, and hornfels in the Saldaña Formation show long NNW-SSE sub-horizontal fractures and fracture corridors with NW-SE directions. Also, in the northwestern portion of Zone 2, there are NW-SE striking faults and fractures affecting the Saldaña Formation (Fig. 4d).

The western part of the hanging-wall of the Agrado-Betania fault (Zone 3; Fig. 2a) is characterized by high-angle fractures trending N–S, which are associated with minor faults striking in the same direction (Fig. 4d). Finally, Zone 4 (Fig. 2a) encompasses the core of a transverse fault, with NW-SE strike and moderate dip angle (~35–40°), which is characterized by pervasive chlorite-epidote-sericite mineralization concentrated along cataclasite planes. Kinematic indicators, like slickensides and conjugate sets of fractures, indicate a strike-slip component for this fault that controls the orientations of structures in this location (Fig. 4d).

4.3.2. Evaluation of the fault damage zone

The three fault architectural elements of the Agrado-Betania fault were observed, including the fault core, the damage zone, and the host rock. The core experienced higher deformation intensity than the damage zone, and therefore, as the core approaches, the basement rocks exhibit higher fracture intensities. The Agrado-Betania fault core is characterized by non-foliated crackle breccias and cataclasites, composed of fragments of volcaniclastic rocks from the Saldaña Formation (Fig. 6a). The core has a thickness of ~40 m. The core of the Agrado-Betania fault is bounded by the damage zone, which consists of highly fractured rocks with limited textural and compositional modifications. Also, the damage zone is defined by ordered sets of fractures and secondary minor faults (Fig. 4c and 6a). Secondary minor faults, identified through remote sensing and field data, are associated with the regional Agrado-Betania fault. These structures are mainly oriented NW-SE and NNW-SSE(Fig. 4c). Finally, the host rock is represented by a low fracture intensity zone (Fig. 6a).

Cumulative frequency of P_{10} fracture intensity through the change between the slopes on the hanging-wall was used to calculate a width of ~746 m for the damage zone of the Agrado-Betania fault (Fig. 6a; Choi et al., 2016). The boundary of the damage zone can also be observed by the decrease from ~50 fractures/meter to less than 10 fractures/meter in the host rock at ~1000 m from the fault core (Fig. 6a). Tuffs are located in both damage zone and host rock; therefore, the reduction of fracture intensity is mainly associated with structural position (Fig. 6d and e).

Structural observations from twenty-two field stations are used to evaluate the relationship between P_{10} and P_{21} fracture intensities with distance from the Agrado-Betania fault core. The linear fracture intensity (P_{10}) diagram, as well as the areal fracture intensity (P_{21}) show a clear reduction as the distance from the fault core increases (Fig. 6b and 7c). To estimate this relationship, we computed a regression of both fracture intensities (P_{10} and P_{21}) against fault distance, getting an inverse power-law distribution. For P_{10} values, the distribution is portrayed by Equation (4.1), with an $R^2 = 0.68$ (Fig. 6b).

$$P_{10} = 2744 * (fault\ distance)^{-0.771} \quad (4.1)$$

Likewise, the distribution of the P_{21} values is represented by Equation (4.2), with an $R^2 = 0.81$ (Fig. 6c).

$$P_{21} = 2530 * (fault\ distance)^{-0.69} \quad (4.2)$$

The boundary of the calculated damage zone through cumulative frequency methodology coincides graphically with the maximum curvature point of the power-law distribution, which confirms ~750 m of width for the Agrado-Betania damage zone.

4.3.3. Fracture intensity

To compare the effect of lithology and diagenesis in fracture development, field stations were separated between the damage zone and host rock, according to the width calculation presented in the previous sub-section. We performed scanlines and circular scanning windows in eight stations within the damage zone and fifteen within the host rock. Results were integrated to correlate the average intensity of deformation (P_{10} and P_{21}) with the simplified lithologies. Fracture analysis, including topology, intensity, porosity, and permeability are summarized in Table 2. This approach enables the estimation of the average brittle structure intensity by each integrated lithofacies, allowing the identification of the changes between the damage zone and host rock. Also, the influence of rheology in fracture development was evaluated through this approach.

P_{10} fracture intensity within the damage zone ranges from ~11.2 fractures/m to 64.0 fractures/m, while in the host rock P_{10} fracture intensity values are below ~20 fractures/m (Fig. 6b and 7). Areal fracture intensity P_{21} displays a similar pattern, ranging from ~25.2 m/m^2 to 136.6 m/m^2 in the damage zone, and reaching values lower than ~31.5 m/m^2 in the host rock (Fig. 6c and 8).

Table 2
Summary of the obtained results in the fracture analysis. Fracture orientation results are presented in Table S1, and fracture apertures measured on outcrops are presented in Table S2, matrix porosity and permeability are shown in Table S3. C_B: average connections per branch; P_{10}: 1-D frequency (# fractures/m); P_{21}: areal fracture intensity (m/m^2).

Station	Longitude	Latitude	Lithology	Structural position	Distance to fault (m)	Y Nodes	X Nodes	I Nodes	P10 (# fractures/m)	P21 (m/m2)	CB	Fracture porosity with minimum aperture (%)	Fracture permeability with minimum aperture (mD) (Tiab and Donaldson, 2015)	Fracture porosity (%) (Marrett, 1996)	Fracture permeability (mD) (Marrett, 1996)
Ag-02-2	−75.7141	2.3308	Volcanic lithic breccia	Damage zone	370	76	14	121	45.0	50.9	1.4	0.34	1811.4	1.5	424578.8
Ag-02-3	−75.7145	2.3306	Shard-rich rhyolitic ash tuff	Damage zone	386	198	8	180	51.8	55.9	1.6	1.88	87884.9	4.5	7364131.1
Ag-04	−75.7171	2.3292	Tuffaceous conglomerate	Damage zone	529	151	12	99	23.0	26.3	1.7	3.81	529.0	2.3	3405803.7
Ag-06	−75.7170	2.3279	Shard-rich rhyolitic ash tuff	Damage zone	396	231	21	293	32.1	53.4	1.5	1.09	563.2	2.3	1700179.0
Ag-07	−75.7170	2.3279	Volcanic lithic breccia	Damage zone	456	211	30	207	11.5	25.2	1.6	0.53	11423.7	0.8	767628.7
Ag-09	−75.7223	2.3246	Shard-rich rhyolitic ash tuff	Damage zone	715	39	0	60	25.0	29.9	1.3	0.70	2166.2	1.3	373117.3
Ag-10	−75.7233	2.3218	Crystal rhyolitic ash tuff	Damage zone	660	433	115	212	64.0	136.6	1.8	1.11	9891.2	2.6	302058.9
Ag-20	−75.7311	2.3098	Volcanic lithic breccia	Damage zone	482	190	30	165	11.2	30.5	1.6	0.54	2208.5	0.8	618318.0
Ag-46	−75.7314	2.3278	Shard-rich rhyolitic ash tuff	Host rock	1934	171	10	110	10.7	6.6	1.7	0.78	12760.8	0.6	375682.6
Ag-11	−75.7264	2.3187	Crystal qz-trachyte tuff	Host rock	801	120	8	165	17.8	31.5	1.4	1.87	4045.6	1.0	604925.7
Ag-16	−75.7335	2.1380	Crystal qz-trachyte tuff	Host rock	1023	83	14	25	13.1	26.4	1.8	1.90	2229.5	0.7	282980.0
Ag-48	−75.7307	2.3251	Crystal rhyolitic ash tuff	Host rock	1570	129	22	84	9.2	13.9	1.7	10.53	11694.8	0.5	292566.3
PCAg-48	−75.7311	2.3233	Shard-rich rhyolitic lapilli tuff	Host rock	1514	128	25	27	8.0	13.0	1.9	6.73	942.0	0.2	18227.4
Ag-24	−75.7444	2.3237	Hornfels (sedimentary breccia)	Host rock	2683	58	3	63	2.1	4.7	1.5	0.90	608.8	0.1	160748.7
Ag-25	−75.7445	2.3237	Hornfels (Crystal qz-trachyte ash tuff)	Host rock	2641	347	68	272	10.5	20.5	1.7	0.23	17234.3	0.9	3068636.8
Ag-26	−75.7437	2.3240	Hornfels (Crystal qz-trachyte ash tuff)	Host rock	2664	118	19	131	7.9	11.2	1.5	1.44	808.9	0.4	162360.7
Ag-27	−75.7447	2.3226	Qz-monzodiorite	Host rock	3350	38	19	13	5.7	6.7	1.9	0.33	5602.4	0.3	360702.5
Ag-29	−75.7468	2.3382	Qz-monzodiorite	Host rock	3858	30	9	21	7.2	12.2	1.7	0.08	1573.0	0.2	11296.5
Ag-29 (2)	−75.7468	2.3382	Qz-monzodiorite	Host rock	3865	48	4	22	5.2	9.4	1.8	0.06	1202.5	0.2	42880.5
Ag-30	−75.7455	2.3423	Qz-monzonite	Host rock	3940	110	10	124	9.3	14.0	1.5	0.54	42618.1	0.8	2505129.5
Ag-37	−75.7343	2.3376	Crystal qz-trachyte tuff	Host rock	2595	–	–	–	3.0	–	–	–	–	–	–
Ag-44	−75.7324	2.3326	Crystal rhyolitic ash tuff	Host rock	2165	–	–	–	9.0	–	–	–	–	–	–
Ag-41	−75.7346	2.3345	Shard-rich rhyolitic ash tuff	Host rock	2450	92	15	150	3.0	13.1	1.4	0.02	263.4	0.2	34483.6

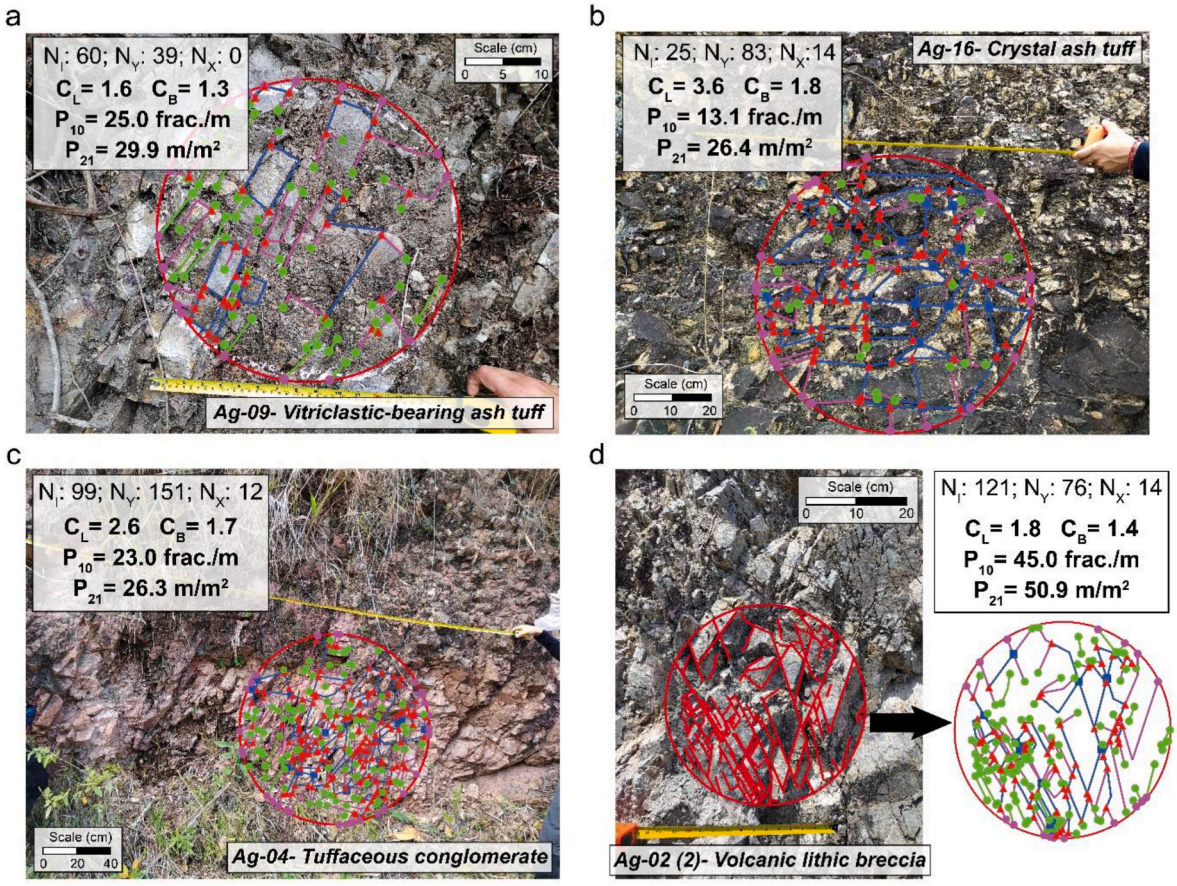

Fig. 7. Field measurements of the fractured rocks within the Agrado-Betania fault damage zone. a) Vitriclastic-bearing ash tuff with high fracture intensity and low connectivity; b) Crackle breccia after crystal ash tuff displaying high fracture intensity and high connectivity. c) Well-connected tuffaceous conglomerate with high fracture intensity; d) Volcanic lithic breccia showing high fracture intensity with low connectivity. Green dots represent isolated nodes (I), red triangles abutting nodes (Y), and blue squares connecting nodes (X). Also, the isolated branches (I–I) are represented by green lines, partially connected (I–C) by light violet lines, and totally connected (C–C) by blue lines. For a better interpretation of the conventions, refer to Fig. 3.

Some rheological differences on fracture intensity between lithologies were recognized. Volcanic breccias and ash tuffs display fracture intensities slightly higher than quartz-monzodiorites, hornfels, and tuffaceous conglomerates in the damage zone as well as in the host rock (Fig. 6d and e). These differences are more evident in the P_{21} diagrams (Fig. 6e and 7). The average of fractures linear intensity (P_{10}) in the damage zone has values of 24.6 fractures/m, 23.5 fractures/m, and 23.2 fractures/m for volcanic breccia, crystal ash-tuff, and tuffaceous conglomerate, respectively, while shard-rich ash-tuff has a lower value of 17.7 fractures/m. Additionally, P_{10} intensity in host rock shows lithological variations: volcanic breccia, shard-rich ash-tuff, shard-rich-lapilli tuff, hornfels, crystal ash-tuff, and quartz-monzodiorite with values ranging between 9.2 fractures/m and 5.6 fractures/m (Fig. 6d and 8). Similarly, P_{21} intensity values for crystal ash-tuff (64.8 m/m^2), shard-rich ash-tuff (46.4 m/m^2), and volcanic breccias (35.5 m/m^2) are slightly higher than tuffaceous conglomerate (26.3 m/m^2) in the damage zone. In the host rock volcanic breccias, P_{21} has values of 20.2 m/m^2, while in the other lithologies it ranges from 9.9 m/m^2 to 13.9 m/m^2 (Fig. 6e and 8).

4.3.4. Fracture connectivity

Fracture connectivity was estimated in eight stations within the damage zone and thirteen stations within the host rock. The results of connection per branch (C_B) were plotted on triangular diagrams representing nodes and branches, with stations categorized by lithology (Fig. 9a and b). Additionally, the C_B index was compared to fault distance using a scatter plot (Fig. 9c).

The topological analysis reveals that both the damage zone and host rock stations have high connectivity, as indicated by the significant proportion of C–C branches and the prevalence of X and Y nodes (Fig. 9a and b). The connectivity surpasses the $C_B = 1.5$ percolation threshold established by Sanderson and Nixon (2018), with only four stations falling below this threshold (Fig. 9). Furthermore, the connectivity diagrams exhibit high scattering, suggesting a weak relationship between fracture connectivity, fault distance, and lithology (Fig. 9c).

4.4. Petrophysics

4.4.1. Matrix porosity and permeability

Porosity and permeability were measured from 22 core plugs sampled in 17 field stations from the Saldaña Formation and the Astillero Pluton, including crystal to shard rich ash and lapilli tuffs with rhyolitic to trachytic composition, volcanic lithic breccias, tuffaceous conglomerates, hornfels, and quartz-monzodiorites (Table S3).

The average matrix porosity is 1.7% and there is not a clear relationship with the fault core position. However, a rough lithological control in porosity can be observed; for instance, tuffaceous conglomerate, ash tuffs, and lapilli tuffs show higher values, ranging from 0% to 10.3%, than volcanic breccias, hornfels, and plutonic rocks, which only achieve values lesser than 1.4%. Additionally, most core samples exhibited very low permeabilities, where only three samples of crystal ash tuffs displayed permeability measurements ranging from 0.02 mD to 9.22 mD (Table S3).

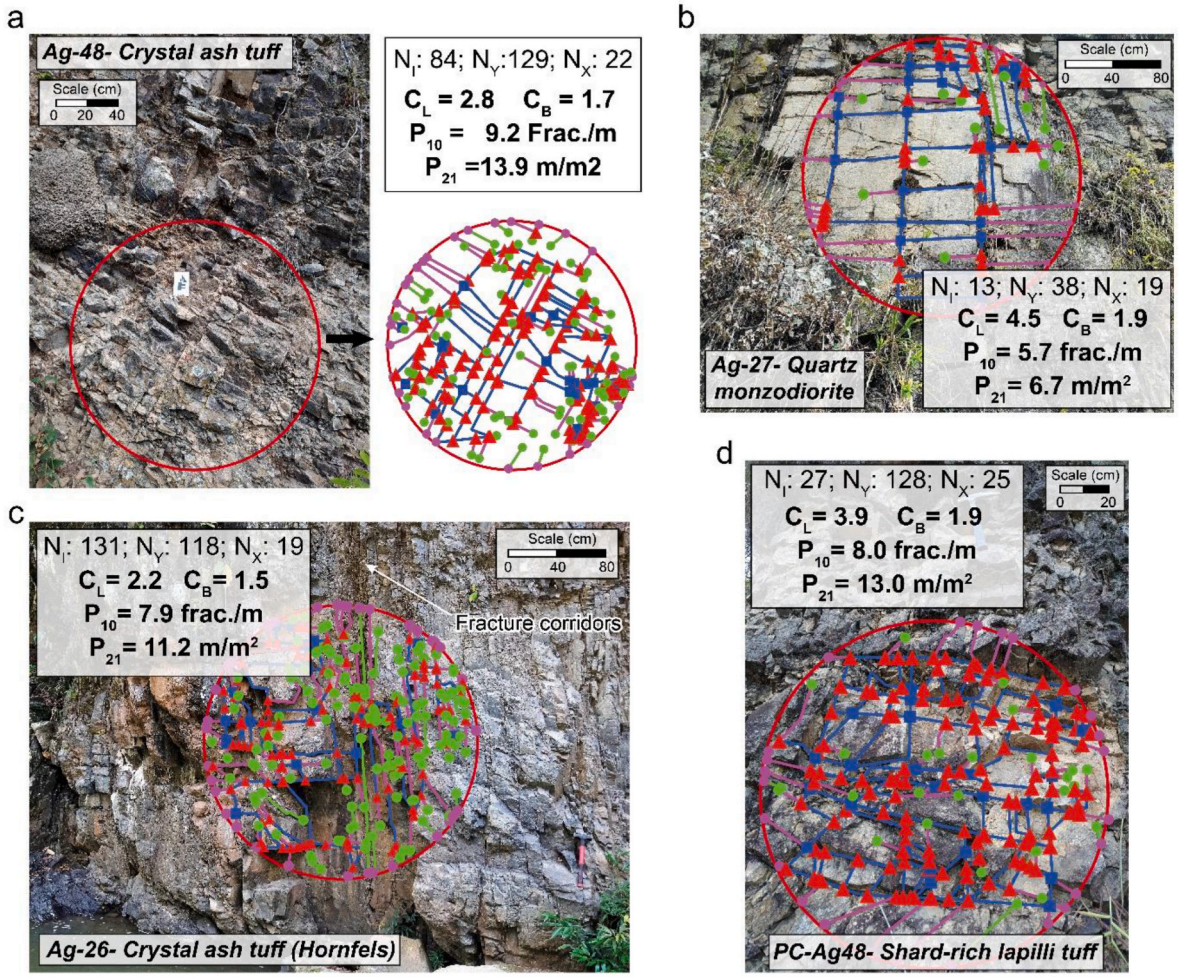

Fig. 8. Field measurements of the fractured rocks within the Agrado-Betania fault host rock zone. a) Crystal ash tuff showing moderate-to-low fracture intensity and high connectivity; b) Well-connected quartz-monzodiorite from the Astillero Pluton displaying low fracture intensity. c) Hornfels after crystal ash tuff with moderate fracture intensity and connectivity. Note the fracture corridors produced by near-vertical fracture sets; d) Shard-rich lapilli tuff with high connectivity and moderate fracture intensity. Conventions as in Fig. 7.

4.4.2. *Fracture porosity and permeability*

The results of fracture porosity and permeability were plotted on a scatter diagram to make comparisons with reservoir characteristics of the volcanic rocks pore-fracture units of the Yingcheng Formation, which is located in the south-eastern part of the productive Songliao Basin in China (Tang et al., 2022), and the Shiranish Formation in the Taq Taq Field, Kurdistan Region of North Iraq (Rashid et al., 2023).

The Yingcheng Formation was chosen for the analysis due to the available data and the similar volcanic lithofacies found in Saldaña Formation, whereas the Shiranish Formation was select as it presents results of a fractured reservoirs under well pressure conditions. We also include available data from the Barco and Mirador formations in the Llanos region of Colombia as they show similar diagenetic properties of the Jurassic volcaniclastic rocks, such as compaction and quartz cementation.

By using the Tiab and Donaldson's equation with mean aperture and the Marrett's method, we obtained permeability values ranging from 9816.0 mD to 7364131.1 mD, while fracture porosity displayed values, ranging from 0.1% to 5.0% (Table 2 and Fig. 10). Nevertheless, the matrix porosity of some lithofacies, such as crystal ash tuff and shard-rich lapilli tuff, improved the general porosity of the outcrops, where at least two stations reached values higher than 5.0% (Fig. 10).

We also obtained minimum values of effective permeability and dual porosity, which range from 79.0 mD to 26365.5 mD and 0.1%–3.2%, respectively (Fig. 10). Considering the minimum aperture at each outcrop, the results were subsequently reduced by 70% (Rashid et al., 2023).

Porosity and permeability values of the Saldaña Formations on outcrops display higher values than the Yingcheng Formation in China; the Shiranish Formation in the Taq Taq Field, Kurdistan Region of North Iraq; and the Barco and Mirador formations in the Cusiana Field, Colombia(Fig. 10). However, by using the minimum aperture and the reduction of values by 70%, the results of the studied outcrop analog reached are similar to the Taq Taq Field (Iraq) and the Cusiana Field (Colombia) (Fig. 10).

4.5. *Low-temperature thermochronology*

Two samples of quartz-monzodiorite composition were collected between 1200 and 1300 m.a.s.l. in a short transect within the Astillero Pluton in the hanging-wall of the Agrado-Betania Fault. The zircon and apatite fission-track data and single zircon and apatite helium data are summarized in Table 3 and Table 4, respectively. AFT and ZFT samples passed the chi-square test (Table 3), suggesting that single-grain ages for each sample likely belong to the same population.

ZFT from sample 34029Bz yields an age of 124.7 Ma ±1.9 Ma (Fig. 2a). AHe and ZHe data were also obtained in this sample. AFT from the upper sample (34029Bz) yields an age of 46.0 Ma ±3.4 Ma whereas the sample collected at the lower elevation has an age of 19.6 Ma ±1.4 Ma associated with a mean track length of 13.1 μm ± 1.4 μm.

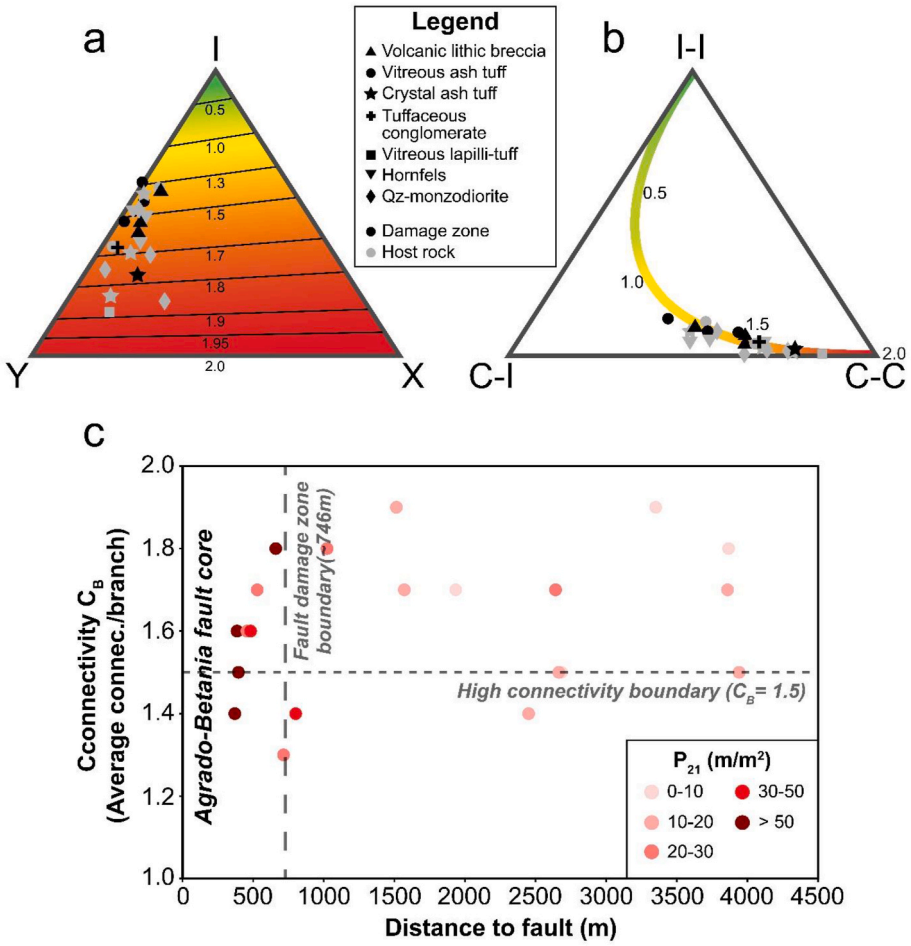

Fig. 9. Summary of fracture connectivity analysis results in the hanging-wall of the Agrado-Betania fault. a) Ternary diagram of the I, X, and Y nodes distribution showing the C_B values for fault damage zone and host rock plotted by lithology (Nyberg et al., 2018); b) Ternary diagram of the I–I, C–I, and C–C branches distribution plotted by lithology (Nyberg et al., 2018); c) Relationship between fracture connectivity (C_B) and fault core distance classified by P_{21} fracture intensity.

ZHe ages vary between 85.4 Ma and 22.2 Ma whereas AHe single grain ages are between ~13.0 Ma and 63.0 Ma, no clear intra-sample eU or size trend were observed.

For modeling, two AHe corrected reproducible ages overlapping around 13 Ma and the two ZHe corrected ages of 85.4 Ma ±4.0 Ma and 67.0 Ma ±1.4 Ma were included in the model, with the younger age of ~22 Ma excluded. The anomalously young, excluded ages may be the result of unidentified U zonations, helium implantation, and high helium micro-inclusions (Farley, 2002; Murray et al., 2014).

The inverse thermal history model exhibits an Early Cretaceous cooling event from below the ZFT partial annealing zone up to surface temperatures, as suggested by the overlying Cretaceous strata. Afterwards, these blocks experienced a reheating event within the zircon helium partial annealing zone at 90 Ma followed by Late Cretaceous cooling. After a Paleogene re-heating episode, a final cooling event occurred around 20 Ma (Fig. 11).

5. Discussion

Multi-scale evaluation of brittle deformation, including the integration of topographic lineaments together with outcrop structural analysis, petrographic descriptions, and low-temperature thermochronology enable us to reconstruct the style, distribution, and timing of the deformational phases and the reservoir attributes of the Agrado-Betania fault in the southern UMVB.

We will start discussing the tectonic implications of our findings, highlighting the significance of superimposed deformation events and inherited features in basement rocks. Subsequently, we will address considerations regarding the architecture of the Agrado-Betania fault, discussing the main factors controlling the distribution of brittle deformation. Finally, we will mention the principal characteristics of the fractured system that could enhance the reservoir quality in fractured crystalline rocks and the implications that these results would have in hydrocarbon exploration in the Upper Magdalena Valley Basin.

5.1. Tectonic implications

The UMVB presents a long-term sedimentary record from the Early Cretaceous to present day. Different tectonic episodes have affected the basin, such as extensional regimes during the Early Cretaceous that changed to a contractional regime during the Cretaceous and the Cenozoic. Due to this deformational history, different thrust faults were nucleated and evolved as a result of the reactivation of inherited structures in a thick-skinned deformation style (Anderson et al., 2016; Espitia et al., 2022; Jiménez et al., 2012; Mora et al., 2010; Rosero et al., 2022; Saeid et al., 2017; Villamizar-Escalante et al., 2021).

Our multi-scale analysis shows that the Agrado-Betania and La Plata-Chusma faults have a NE trending with associated NW and N–S-trending strike-slip faults (Figs. 4c and 5d). The presence of NW structures in the UMVB has been previously documented by other researchers, who interpreted them as inherited faults from the pre-Cretaceous and Early Cretaceous extensional regimes (Jiménez et al., 2012; Ramon and Rosero, 2006, and references therein). These NW structures have been interpreted as extensional transfer structures based on the lateral change

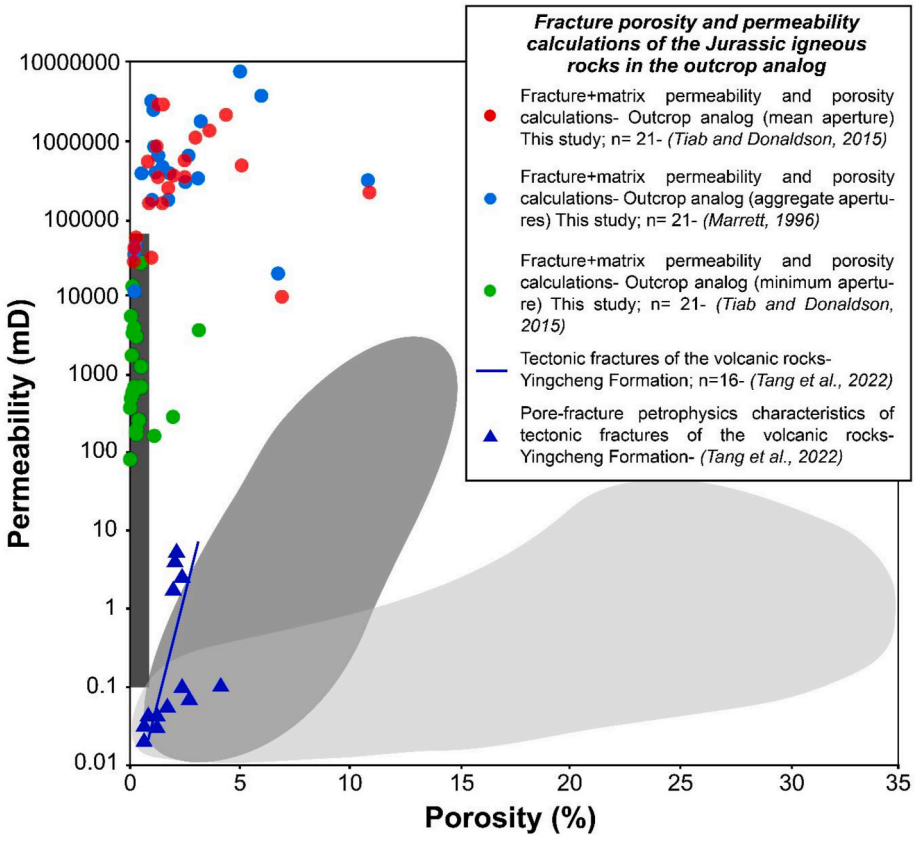

Fig. 10. Porosity and permeability calculations conducted in Jurassic igneous rocks exposed in the hanging-wall of the Agrado-Betania fault. The results include both fracture and matrix porosity and permeability. The light-gray shaded area represents the primary porosity of the Yingcheng Formation volcanic rocks in wells Y1D1 and Y3D1 in the Songliao Basin, China (Tang et al., 2022). The medium-gray shaded area represents the porosity and permeability values of the fractured tight-cemented quartz-arenites from Barco and Mirador formations in the Cusiana Field, Llanos Basin Foothills, Colombia (Cazier et al., 1995). The dark-gray area portraits the porosity and permeability values for core plug samples from the Shiranish Formation in the Taq Taq Field, Kurdistan Region of North Iraq (Rashid et al., 2023).

of thickness of Caballos and Villeta formations and the segmentation of deformation along strike in the southern part of the UMVB (Jiménez et al., 2012).

The existence of multiple deformational events is supported by thermochronological data, which indicate a polyphasic deformation history in the hanging-wall of the Agrado-Betania fault, consisting of at least three exhumation episodes (Fig. 11). The thermochronological data suggest Early Cretaceous cooling supported by a ZFT age of 124 Ma. This exhumation event is also supported by the angular unconformity of the Saldaña Formation with the Caballos Formation, which implies the exhumation of the Astillero pluton and tilting of the Saldaña Formation between ~140 and 125 Ma. This event aligns with an Early Cretaceous (140-100 Ma) extensional event recorded throughout the UMVB (Bayona, 2018; Carvajal-Torres et al., 2022; Mora et al., 2006, 2009, 2010; Sarmiento-Rojas, 2019).

We propose a connection between the first Early Cretaceous exhumation period (140-100 Ma) and the extensional regime experienced by the UMVB during that time; this may imply that the Agrado block was probably undergoing extensional exhumation. This means that the Agrado block was the footwall of a major normal fault to the west, such as the La Plata-Chusma Fault; the activity of the Agrado fault during this period remains unknown.

The reheating of at least 120 °C, between 110 Ma and 90 Ma, observed in the Agrado block also suggests that after exhumation, the Agrado-Betania fault and/or other fault to the east had a normal behavior facilitating sediment accumulation (Anderson et al., 2016; Espitia et al., 2022; Jiménez et al., 2012; Mora et al., 2010; Saeid et al., 2017; Villamizar-Escalante et al., 2021).

The thermochronological data reveal two additional periods of exhumation, one in the Late Cretaceous (~70 Ma) and another during the Oligocene-Early Miocene (~25 Ma). The seismic interpretations in the south of the UMVB (Neiva Sub-basin) lack of any angular unconformity or syn-tectonic strata between the early Eocene and early Miocene, suggesting that despite the onset of deformation and exhumation occurred during the late Oligocene and the early Miocene, major uplift occurred after deposition of the upper Miocene units (Espitia et al., 2022). These late phases of uplift and deformation may not be recorded by the thermochronological data, likely because they were related to low exhumation due to the exposure of a crystalline basement more resistant to erosion (Sobel and Strecker, 2003; Zapata et al., 2019b). These late Miocene deformation events are also evidenced by the thrusting relationship between the Jurassic Saldaña Formation and the upper Miocene volcaniclastic Gigante Formation (~8 Ma), located in the footwall of the Agrado-Betania fault (Fig. 2; Espitia et al., 2022).

Our data suggest that basin inversion started during the Late Cretaceous (~70 Ma). Extensive intra-basinal deformation between the Late Cretaceous-Paleogene and the Eocene is well documented in a pronounced regional unconformity that characterized several basins in eastern Colombia (Cooper et al., 1995; Gómez et al., 2003, 2005; Espitia et al., 2022; Parra et al., 2012; Ramon and Rosero, 2006).

We suggest that the chlorite and sericite mineralization could have probably been developed during the Early Cretaceous extensional deformation, contemporary with hydrothermal activity. Then, contractional phases generated the open fractures, which are superimposed on the previous mineralization. These contractional phases promoted fracture development in the Agrado-Betania fault, resulting in the

Table 3
Zircon and apatite fission-track data. Complete single-grain data is presented in Table S4. N[a]: number of grains; Ns: number of spontaneous tracks; Ni: number of induced tracks; Nd: number of tracks during dosimetry; RhoD: dosimeter track density; P(X)d: Chi-square; Ne: number of grains with length of tracks; MLT: Average track length; SD: Standard deviation; ζ: Zeta number of the analyst.

Sample code	Latitude	Longitude	Mineral	Nb	Ns	Ni	Nd	RhoD (x105)c	Age (Ma)	±1σ (Ma)	P(χ)d (%)	Ne	MTL (μm)	SDf (μm)	Dpar (μm)	SDg (μm)	ζ (zeta)	±2σ
34029BZ	2.3431	−75.746	Ap	26	253	998	18252	36.3608	46.0	3.4	15.3	Na	Na	Na	2.45	0.30	100	1.9
34031BZ	2.3327	−75.745	Ap	19	251	2316	18252	36.2401	19.6	1.4	51.4	23	13.1	1.4	2.24	0.18	100	1.9
34029Bz	2.3431	−75.746	Zr	29	2531	201	9354	1.23763	124.7	9.9	99.4	Na	Na	Na	Na	Na	161	4.4

b Dosimeter track density.
c Pooled age.
[a] Number of counted grains.

formation of the architectural elements such as fault core and fault damage zone.

In the Garzón Massif, at the eastern boundary of the UMVB, thermochronological ages in the basement suggest a history of exhumation during the Mio-Pliocene (12.5 Ma - 3.6 Ma), possibly associated with the activity of the Algeciras fault in the Eastern Cordillera (Anderson et al., 2016). Additionally, the evolution of the Eastern Cordillera may have played a significant role in the final configuration of the basin, causing greater internal deformation and favoring thick-skin deformation (Saeid et al., 2017).

The width of the damage zone and the total displacement of a fault have a proportional relationship, which can vary according to lithology, fault type, and fault segment interactions (Choi et al., 2016; Hansberry et al., 2021; Kim et al., 2004; Lin and Yamashita, 2013; Peacock et al., 2017a, 2017b). For instance, Celestino et al. (2020) calculated the best-fit equation $Y = 0.69\ X^{0.74}$.

The footwall of the Agrado-Betania fault comprises approximately 4–5 km of Meso-Cenozoic sedimentary rocks, which were likely eroded from the hanging-wall, exposing the Jurassic basement of the basin. Additionally, as the latest cooling episode starts at 25 Ma from about 120 °C, we can calculate a minimum exhumation (fault throw), assuming that there are no hydrothermal modifications in the basin. Therefore, considering a geothermal gradient between 25 and 30 °C/km and a surface temperature of 20 °C, thermal data suggest around 4 km of Miocene exhumation relative to the adjacent basin. These calculations are supported by seismic data that suggest a minimum fault throw of about 4–5 km (Espitia et al., 2022). To estimate the total displacement of the Agrado-Betania fault, including vertical and horizontal movement, we used the aforementioned equation along with the width of the damage zone (Fig. 6a). A damage zone width of approximately 746 mis expected to have a displacement of 12 km, which is significantly greater than the Miocene displacement estimates derived the sedimentary thickness and the thermochronological data. Thus, we propose that the additional 7–8 km of displacement may be attributed to fault movements related to previous deformation events, as suggested by the thermochronological data (Fig. 11). Furthermore, considering the dextral strike-slip component of the Agrado-Betania fault (Diederix et al., 2020), the total fault displacement can also be achieved through lateral movement during Cretaceous to Miocene deformation events.

5.2. Fault architecture and its relations with brittle deformation heterogeneity

Numerous studies have established a clear correlation between topographic lineaments and the presence of geological structures at regional scales (Celestino et al., 2020; Cianfarra and Salvini, 2015; Rahiman and Pettinga, 2008; Wise et al., 1985). Our research has enabled the identification of regional fault zones where lineament intensity (highlighted in red in Fig. 4c) aligns parallel to the trends of the regional faults, particularly in the hanging-wall of the La Plata-Chusma and Agrado-Betania faults. However, some NW trending patterns with high lineament intensity are observable in the hanging-wall of the Agrado-Betania fault (Fig. 4c), which can be explained by the presence of secondary NW-SE and NNW-SSE striking faults, which were observed in the field and their orientations were measured in different outcrops (Fig. 4c and d). These minor faults could be enhancing the brittle deformation in the host rock zones.

While the “off-fault” areas with high lineament intensity from the La Plata-Chusma and Los Frailes Faults could potentially be linked to secondary NW-SE and NNW-SSE striking faults with complex linking fault damage zones (Kim et al., 2004; Peacock et al., 2017a, 2017b), the absence of outcrop data in these regions precludes the possibility of confirming these relationships.

We observed slight variations in deformation intensity from west to east, with a gradual decrease in lineament intensity towards the east (from ~0.02 m/m2 to ~0.002–0.016 m/m2, Fig. 4c). This spatial

Table 4
Single zircon and apatite helium data. The reported data are ZHe and AHe corrected ages. U: uranium concentration; Th: Thorium concentration;^{147}Sm: Samarium concentration; He: Helium concentration; Ft: Ft correction; ESR: equivalent spherical radius; Term: number of terminations.

Sample code	Mineral	Age (Ma)	±1σ (Ma)	U (ppm)	Th (ppm)	147Sm (ppm)	He (nmol/g)	mass (ug)	Ft	ESR (um)	Term
34029BZ-a1	Ap	14.2	0.8	12.3	23.4	95.6	1.0	1.4	0.70	50.9	2.0
34029BZ-a2	Ap	63.3	2.3	6.8	15.0	75.1	2.7	1.4	0.70	49.3	1.0
34029BZ-a3	Ap	13.5	0.5	28.6	48.5	111.9	2.3	1.5	0.80	55.7	1.0
34029BZ-a4	Ap	23.6	1.1	10.8	37.2	69.8	1.9	1.4	0.70	47.2	0.0
34029Bz-z1	Zr	85.4	4.04	1.59	5.0	5.5	1.0	5.25	0.79	57.07	2.0
34029Bz-z2	Zr	67.0	1.34	72.41	102.3	1.4	26.9	3.41	0.77	49.57	2.0
34029Bz-z3	Zr	22.2	2.52	3.67	42.8	22.0	1.3	3.33	0.75	48.74	2.0

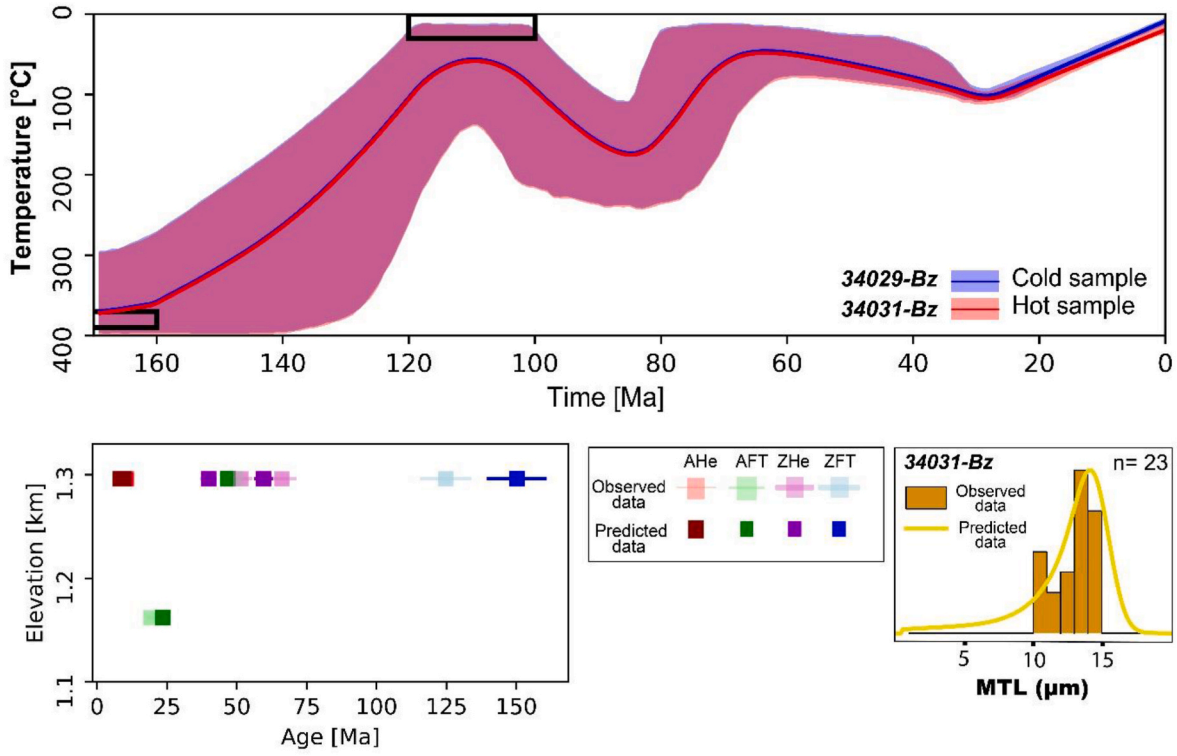

Fig. 11. Inverse thermal history models were generated using bedrock data acquired in the hanging-wall of the Agrado-Betania fault. The upper panel displays the thermal histories, along with 2-sigma confidence intervals, for both cold-sample (blue) and hot-sample (red). On the lower panel, observed and predicted data are shown. The thermochronological system is indicated by marker color and shape, while light colors represent the observed data. The inverse thermal history models were conducted using uncorrected He ages.

distribution could be related to a higher structural level reached by the tectonic block located in the Central Cordillera, which was exhumed through the La Plata-Chusma fault due to a possible long-term deformation history and also the major magnitude of deformation associated with more fault displacement. This idea finds further support in the differences in magmatic rocks exposed along both faults, with deep-crust plutonic rocks exposed along the La Plata-Chusma fault and shallow-crust volcanic facies exposed in the hanging-wall of the Agrado Fault (Butler and Schamel, 1988; Jiménez et al., 2012; Villagómez et al., 2011; Villamizar-Escalante et al., 2021).

P_{10} and P_{21} fracture intensity values can be used to evaluate the effects of lithology and structural position. Results showed that volcanic rocks, such as volcanic breccias and ash tuffs have a slightly higher degree of fracturing than tuffaceous conglomerates and quartz-monzonites (Fig. 6d and e). This difference could be explained by the presence of more brittle minerals in volcanic rocks, such as glass with devitrification, feldspar, and quartz, while tuffaceous conglomerates are pumice-rich, which have a more plastic response to deformation (Mousavi and Bryant, 2013; Sun and Zhong, 2018 Wei et al., 2020; 2022). The isotropic nature of the plutonic rocks and the content of mafic minerals could be the main factor producing low fracture intensities and resulting in rather long and spaced fractures.

Although it was possible to observe some differences in fracture intensity between lithologies, these differences are not as significant as seen in other volcanic examples (Jiang et al., 2017; Sun and Zhong, 2018). We suggest that the intense diagenetic process and the silicification undergone by Jurassic igneous rocks of the Saldaña Formation (Fig. 4) caused a homogenization of the mechanical strength of the different lithofacies that turned out to have the same response to the brittle deformation experienced later (Wei et al., 2020, 2022; Laubach et al., 2019; Li et al., 2022; Zhou et al., 2016), and therefore we infer that structural position is the first-order factor controlling the development of high fracture intensities in the hanging-wall of the Agrado-Betania fault (Fig. 6).

Fracture connectivity can be increased in 4 ways: (1) higher fracture intensity; (2) increasing fracture length; (3) higher number of fracture sets; and (4) geometrical arrangement of fractures (Sanderson and Nixon, 2015, 2018). Results of connectivity showed that the majority of the field stations exceed the $C_B = 1.5$ percolation threshold established by Sanderson and Nixon (2018), with only four stations falling below

this threshold (Fig. 9c). Within the damage zone, the high fracture intensity is the main factor that enhances the interconnection between the fracture networks; however, the low connectivity in some stations is the result of the presence of just one sub-parallel fracture set and short fractures, triggering a topology arrangement dominated by type I nodes (Fig. 7a and d).

On the other hand, the host rock zone shows high values of connectivity ($C_B > 1.5$; Fig. 9c) associated with low fracture intensities, thus, the length and geometrical arrangement of fractures are the principal factors increasing the connection between networks (Fig. 8a, b, and 8d). The presence of fracture corridors in some stations could result in low connectivity because connections are limited in a single fracture set, but such fracture corridors could play an important role in acting as fluid migration pathways from depth.

Finally, the development of exhumation horizontal fractures can also improve fracture connectivity, because of their long length. Thus, plutonic rocks and hornfels, which are farther from the Agrado-Betania fault core and where horizontal fractures are well-developed, have better connectivity (Watkins et al., 2018; Sun et al., 2021; Bonato et al., 2022; Wang et al., 2023).

The effects of chemical processes on fractures during diagenetic processes (50°C–200 °C) have been presumed to be slight, but recent studies have documented more profound interactions (Laubach et al., 2019). For instance, field studies and some model results have shown correlations between the amount of cement accumulated during fracturing and fracture size distribution, spatial arrangement, and connectivity in both clastic and carbonate rocks (Hooker and Katz, 2015; Hooker et al., 2011, 2013, 2018; Laubach et al., 2014). Fracturing significantly influences dissolution and precipitation processes within fracture systems, where cementation plays a substantial role in shaping the evolution of both fractures and host rocks. The interconnection between host rock and fracture diagenesis plays a crucial role in the development and evolution of fracture systems.

Despite the demonstrated interplay between fracture development and diagenesis in clastic and carbonate rocks, our understanding of the relationship between volcanic rocks and diagenetic processes remains limited (Wei et al., 2020, 2022). For instance, Laubach et al. (2019) suggest that fractures in diagenetically altered rocks may be effective long-term fluid conduits. Also, in diagenetic settings, fracture-wall cementation may even hold fractures open when loading conditions might otherwise close them (Olson, 2004).

Therefore, in light of our results, we suggest that the long-term diagenetic evolution enhances the fracture systems properties, such as intensity, connectivity, and apertures, in volcaniclastic sequences as similarly occurs in sedimentary rocks. (Laubach et al., 2019). Additionally, because of the intense diagenesis undergone by Jurassic volcanic rocks in tandem with the cementation of some minerals throughout the fracture walls, we propose that fractures may be open and well-connected in the subsurface of the Upper Magdalena Valley Basin.

5.3. Reservoir quality

The temporal framework for the fracture systems in the hanging-wall of the Agrado-Betania fault has significant implications for the petroleum system of the UMVB. It indicates that the fracture networks were formed before the Mio-Pliocene period, during which hydrocarbon generation and migration occurred (Sarmiento and Rangel, 2004). As a result, the high connectivity, intensity, and permeability of these fracture systems, along with their pre-existing nature before oil and gas migration, highlight the importance of Jurassic igneous rocks as a promising target for exploration in fractured basement reservoirs within the Upper Magdalena Valley Basin, Colombia. Furthermore, the current oblique convergence between Nazca and South American Plates results in a NE-SW maximum horizontal stress suggesting that the most plausible open fractures would be the NE striking ones, at least for the fractures that do not exhibit clear evidence of cementation. Nevertheless, Laubach et al. (2004) demonstrated that contrary to widespread expectation, opening-mode fractures that are not aligned concerning modern maximum horizontal compressive stress (S_{Hmax}) may not close due to chemical process, which can account for the resistance of fractures to closure (Laubach et al., 2004). Consequently, the degree of cement fill in natural fractures governs fluid flow instead of fracture orientation (Laubach et al., 2004). Therefore, we suggest that the fracture sets near to the fault core, which display cements such as plagioclase and quartz in the wall of the fracture plane, may not be necessarily oriented parallel or nearly parallel to modern-day S_{Hmax} in the Upper Magdalena Valley Basin. Additional information regarding the chemical history of fractures and the surrounding rock may provide a clearer insight to assess the fractures that could be open to fluid flow in the subsurface.

Overall, matrix porosity and permeability of the Jurassic igneous rocks display very low values (Table S3) as a result of compaction and pervasive silicification undergone during diagenesis. Higher values of porosity (>5%) found in some samples are associated with secondary pores produced by mineral dissolution (Fig. 4). However, fracture analysis led us to calculate a wide damage zone (~746 m), in which the fracture networks are well connected, open, and have high fracture intensity.

Tang et al. (2022) demonstrated the impact of different types of reservoirs pores, such as vesicles, dissolution pores, and tectonic fractures on petrophysical properties. Also, they revealed that permeability of fractured igneous reservoirs increases with porosity (Fig. 10). Our fracture porosity and permeability calculations show similar trends to producing wells in fractured carbonate reservoirs from the Taq Taq Field in North Iraq and conventional reservoirs developed in cemented quartz-arenites from the Cusiana Field in Colombia (Fig. 10; Cazier et al., 1995; Rashid et al., 2023; Tang et al., 2022), suggesting that the studied igneous Jurassic basement has a high potential for fluid flow and accumulation.

Furthermore, our porosity and permeability results are several orders of magnitude above known values in fractured basement reservoirs, probably because the main fault activity was developed after the silicification and mineral segregation related to diagenesis allowing the preservation of open fractures (Fig. 10; Debenham et al., 2019; Ma et al., 2023; Meng et al., 2023; Tang et al., 2022; Walter et al., 2018). Also, brittle deformation associated with the Agrado-Betania fault could have happened in a shallow crustal location, where dissolution contemporaneous with the compression associated with the faulting must be lower, resulting in low rates of re-precipitation of silica locally in the newly formed fractures (Watkins et al., 2018).A recent study of volcanic reservoirs has demonstrated that primary pores associated with the magmatic history of rock generation, such as intra-spherulite microfractures, inter-spherulite microfractures, devitrification pores, and vesicles, constitute the main accumulation spaces in these reservoirs (Zheng et al., 2018). However, diagenesis in volcanic rocks substantially reduces primary porosity due to their ash-rich composition and the presence of glassy fragments and plagioclase, that favors the compaction during progressive burial (Mousavi and Bryant, 2013; Sun and Zhong, 2018; Wei et al., 2020, 2022). Also, it has been demonstrated that precipitation of authigenic minerals by rock-fluid reactions negatively impact the porosity and permeability of mixed rocks reservoirs (Wei et al., 2022). For instance, the predominant clay minerals, which consist of fibrous or lath-like illite and grain-coating chlorite, are found in high abundance, occupying the pore spaces and throats, and exerting a negative influence on permeability, thereby impeding fluid flow within the system (Wei et al., 2022).

Despite the reduction of permeability and porosity, the compaction and silicification resulting from diagenetic alterations enhance the mechanical properties of volcanic rocks, thereby promoting their subsequent fracturing (Laubach et al., 2019; Wei et al., 2022). Li et al. (2022) documented that the uniaxial compression strength and tensile strength

values are different between strongly welded tuffs and weakly welded tuffs, where welded tuffs displayed a more brittle behavior with higher values of strength than the weak tuffs.

Thus, we suggest that the volcanic rocks of the Saldaña Formation experienced significant fracturing as a result of increased compression strength and tensile strength values, which were enhanced by the high degree of welding and elevated compaction undergone by the rocks (Fig. 4f, g, 4h, and 4j).

In Junggar Basin, China, the highest porosity values (1.26%–30.08%, with an average of 9.84%) have been found in pyroclastic rocks, followed by andesites (8.14%) and basalts (5.89%) (Zou, 2017). However, Jiang et al. (2017) demonstrated in the Songliao Basin that rhyolitic and

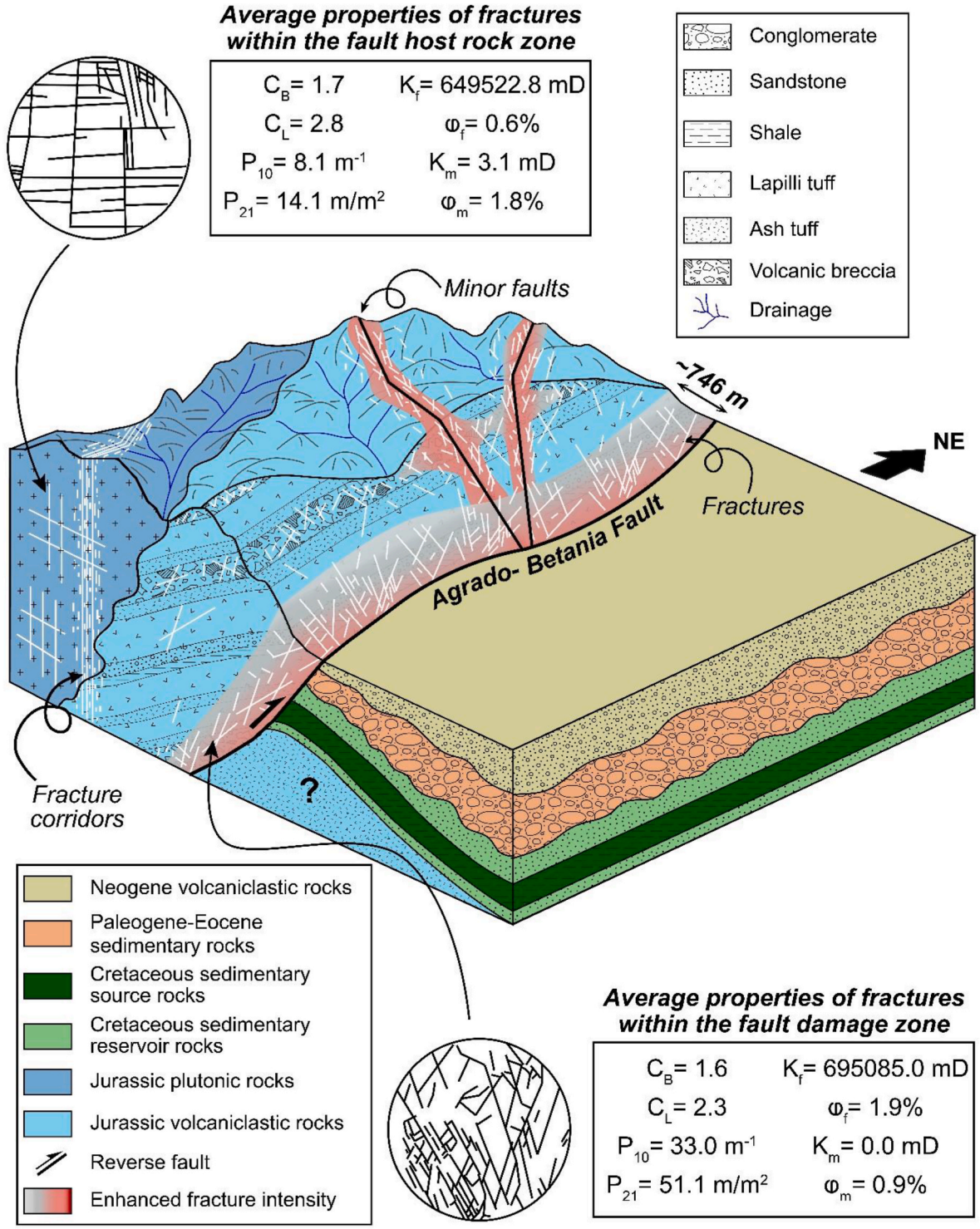

Fig. 12. 3D diagram showing the average of fracture properties within the hanging-wall of the oblique Agrado-Betania fault, enhanced by brittle fault deformation. In the fault damage zone, fractures have high intensity, whereas in the host rock, fractures display lower intensities. Both in the fault damage zone and host rock, fractures have high connectivity and permeability, with low porosity. Also, fractures are mainly open in both zones. There are some places which have fracture corridors that accommodate high strain. Minor faults, within the host rock zone, could be controlling the fracture properties, therefore, enhancing the reservoir quality.

andesitic lithofacies near the crater exhibit higher porosity than pyroclastic breccias and tuffs. Therefore, the quality of a volcanic reservoir can vary significantly, depending on its specific magmatic, diagenetic, and tectonic history. Also, burial can enhance the compaction and diagenesis of rocks, resulting in a significant reduction of matrix porosity and permeability. The pyroclastic facies of the Saldaña Formation in the study area underwent great compaction and silicification due to the Meso-Cenozoic sedimentation, triggering a matrix porosity and permeability decrease.

We conducted an empirical zonation analysis of the outcrop analog in the hanging-wall of the Agrado-Betania fault as a guide for prospectivity of a possible fractured basement reservoir in depth (Fig. 12). Based on the calculated damage zone width (~746 m) and the fracture analysis carried out, we suggest that the areas with more potential to act as fractured basement reservoir include the damage zones associated with regional faults (i.e., seismic scale faults in the subsurface). Additionally, considering that fracture systems develop in the brittle regime of the crust (<7 km depth), we assume that the volume of fractured rock might narrow in depth.

The fault damage zone displays high average fracture intensity ($P_{10} = 33.0$ fractures/m and $P_{21} = 51.1$ m/m^2), and high fracture connectivity ($C_B = 1.6$ and $C_L = 2.3$) (Fig. 12). Furthermore, the host rock zone also exhibits high average fracture connectivity ($C_B = 1.7$ and $C_L = 2.8$) but displays low average fracture intensity ($P_{10} = 8.1$ fractures/m and $P_{21} = 14.1$ m/m^2). However, this fractured area is segmented by minor secondary faults with NW-SE and NNW-SSE orientations which have their own fault damage zones, enhancing the porosity and permeability of the basement rocks, in areas outside the Agrado-Betania damage zone fault (Fig. 12). Therefore, these minor faults could play an important role in hydrocarbon exploration.

Our dual-porosity calculations show that petrophysical properties are mainly controlled by fractures in the damage zone and host rock. Damage zones could reach values of fracture porosity of ~5.0% and permeability of ~1927215.6 mD, in which the average fracture porosity and permeability are 1.9% and 695085.0 mD, respectively (Fig. 12). Host rock zones also reach high average values of permeability (2788526.4mD) and low average values of porosity (0.6%) (Fig. 12). This difference in permeability can be related to the effect of minor faults that extend to the host rock of the Agrado-Betania fault and to the greater fracture heights developed in these zones (see equation (3.6)).

In some places of the hanging-wall of the Agrado-Betania fault, where volcanic lithologies are affected by minor faults, the fracture intensity is greater than for sedimentary and plutonic rocks (Fig. 12). These results suggest a second-order control exerted by differences in mechanical behavior, which could be an important target in fracture reservoir exploration.

However, due to the lithostatic stress experienced by rocks at greater depths, aperture and intensity of fractures can be substantially lower, leading to a significant reduction in accumulation capacity.

In the northern part of the study area, seismic sections show the location of producing wells (i.e., La Cañada Field and Gigante Field) in the footwall of the Agrado-Betania fault system (Fig. 2b: Espitia et al., 2022). Here, it is observed that the Jurassic basement is in contact with the source rocks and reservoir rocks, which could potentially have acted as carriers of hydrocarbons charging the fractured basement. In other parts of the basin the fractured basement is covered by Villeta Group which could act as seal rocks in the hanging-wall of the fault. We suggest that theoretically, all the elements required for the development of a possible fractured hydrocarbon reservoir in the basement of the Upper Magdalena Valley Basin are present.

6. Conclusions

Our integrated approach, conducted in the Jurassic igneous rocks, enabled us to assess the tectono-structural evolution and investigate the primary factors governing the development and spatial distribution of fracture networks along the hanging-wall of the Agrado-Betania fault damage zone. Low-temperature thermochronological data reveals the presence of multiple Cretaceous to Miocene deformational events, which is consistent with our structural data, topographic lineaments, and existing literature. These findings suggest a polyphasic deformation history within the hanging-wall of the Agrado-Betania fault, encompassing at least three exhumation events during which fracture systems were formed.

The results from our outcrop analog show that fracture intensity is mainly controlled by diagenetic history and structural position with a low influence of lithology. small differences between fracture stratigraphy could be related to burial diagenesis suffered by the Saldaña Formation where silicification and compaction resulted in the homogenization of the mechanical properties. Diagenetic evolution enhanced the tensile and contractional strength of volcaniclastic rocks, which favored a more brittle behavior to the later deformation. Also, fracture analysis suggests that high connectivity is mostly controlled by diagenesis, geometry, topology, and type of fractures, instead of lithology or structural position.

Furthermore, petrophysical properties calculation displays permeability values above 1000 mD, while fracture porosity has lower values, ranging from 0.2% to 5.0%. They agree with typical values of fractured hydrocarbon reservoirs in volcanic rocks worldwide.

Consequently, fracture attributes such as high connectivity, intensity, and permeability including their formation before oil and gas migration indicate a high-quality reservoir. These findings highlight the importance of Jurassic igneous rocks located near the regional fault damage zones, where fracture networks are well developed, as a promising target for exploration in fractured basement reservoirs within the Upper Magdalena Valley Basin, Colombia.

Funding

This work was supported by the Colombian Ministry of Science, Technology, and Innovation (Minciencias) and the National Hydrocarbons Agency (ANH) through contract 80740-152-2021 and agreement 785/668-2019.

Declaration of competing interest

The authors declare the following financial interests/personal relationships which may be considered as potential competing interests: Juan Camilo Valencia Gomez reports financial support was provided by Agencia Nacional de Hidrocarburos. Juan Camilo Valencia Gomez reports financial support was provided by Colombia Ministry of Science Technology and Innovation. Sebastian Zapata Henao reports financial support was provided by Agencia Nacional de Hidrocarburos. Sebastian Zapata Henao reports financial support was provided by Colombia Ministry of Science Technology and Innovation. Maryi Rodriguez Cuevas reports financial support was provided by Agencia Nacional de Hidrocarburos. Maryi Rodriguez Cuevas reports financial support was provided by Colombia Ministry of Science Technology and Innovation.

Acknowledgements

This research was conducted as part of the project titled “Structural Modeling and Petrophysical Characterization of the Fractured Crystalline Basement Reservoir Analogue in the Upper Magdalena Valley, Colombia: A New Exploration Opportunity?” which was approved and supported by the Colombia Ministry of Science, Technology, and Innovation (Minciencias) and the National Hydrocarbons Agency (ANH) through contract 80740-152-2021 and agreement 785/668-2019. The project was carried out by the EGEO Research Group (COL0150558) at the National University of Colombia, Medellín. The authors would like to express their sincere gratitude to the members of the EGEO Research Group for their invaluable feedback and constructive input throughout

this research work. Also, we sincerely appreciate the insightful an constructive suggestions provided by the two anonymous reviewers, which have considerably improved the manuscript.

Appendix A. Supplementary data

Supplementary data to this article can be found online at https://doi.org/10.1016/j.marpetgeo.2024.106850.

References

Anderson, V.J., Horton, B.K., Saylor, J.E., Mora, A., Tesón, E., Breecker, D.O., Ketcham, R.A., 2016. Andean topographic growth and basement uplift in southern Colombia: implications for the evolution of the Magdalena, Orinoco, and Amazon River systems. Geosphere 12 (4), 1235–1256. https://doi.org/10.1130/GES01294.1.

Bayona, G., 2018. El inicio de la emergencia en los Andes del norte: una perspectiva a partir del registro tectónico-sedimentológico del Coniaciano al Paleoceno. Revista de La Academia Colombiana de Ciencias Exactas, Fisicas y Naturales 42 (165), 364. https://doi.org/10.18257/raccefyn.632.

Bayona, G., García, D.F., Mora, G., 1994. La Formación Saldaña: producto de la actividad de estratovolcanes continentales en un dominio de retroarco. In: Etayo-Serna, F. (Ed.), Estudios geológicos del Valle Superior del Magdalena. Universidad Nacional de Colombia, pp. 1–21.

Bayona, G., Rapalini, A., Costanzo-Alvarez, V., 2006. Paleomagnetism in mesozoic rocks of the northern Andes and its implications in mesozoic tectonics of northwestern South America. Earth Planets Space: Earth Planets Space 58 (10), 1255–1272. https://doi.org/10.1186/bf03352621.

Bayona, G., Cortes, M., Jaramillo, C., Ojeda, G., Aristizabal, J.J., Reyes-Harker, A., 2008. An integrated analysis of an orogen-sedimentary basin pair: latest Cretaceous-Cenozoic evolution of the linked Eastern Cordillera orogen and the Llanos foreland basin of Colombia. Geol. Soc. Am. Bull. 120 (9–10), 1171–1197. https://doi.org/10.1130/b26187.

Bayona, G., Jiménez, G., Silva, C., Cardona, A., Montes, C., Roncancio, J., Cordani, U., 2010. Paleomagnetic data and K–Ar ages from Mesozoic units of the Santa Marta massif: a preliminary interpretation for block rotation and translations. J. S. Am. Earth Sci. 29 (4), 817–831. https://doi.org/10.1016/j.jsames.2009.10.005.

Bayona, G., Bustamante, C., Nova, G., Salazar–Franco, A.M., 2020. Jurassic evolution of the northwestern corner of Gondwana: present knowledge and future challenges in studying Colombian Jurassic rocks. In: Gómez, J., Pinilla–Pachon, A.O. (Eds.), The Geology of Colombia, 2 Mesozoic, pp. 171–207. https://doi.org/10.32685/pub.esp.36.2019.05. Servicio Geológico Colombiano, Publicaciones Geológicas Especiales 36.

Beltrán, N., Gallo, J., 1968. The Geology of the Neiva Sub-Basin, Southern Portion. Geological Field - Trips. Colombia 1959-1978. Colombian Society of Petroleum Geologists and Geophysicists, Bogotá, pp. 253–275.

Bernet, M., 2009. A field-based estimate of the zircon fission-track closure temperature. Chem. Geol. 259 (3–4), 181–189. https://doi.org/10.1016/j.chemgeo.2008.10.043.

Bonato, J., Wohnrath Tognoli, F.M., Costa Nogueira, F.C., de Miranda, T.S., Inocencio, L. C., 2022. The use of network topology to assess connectivity of deformation bands in sandstone: a quantitative approach based on digital outcrop models. J. Struct. Geol. 161 (104682), 104682 https://doi.org/10.1016/j.jsg.2022.104682.

Bonter, D.A., Trice, R., 2019. An integrated approach for fractured basement characterization: the Lancaster Field, a case study in the UK. Petrol. Geosci. 25 (4), 400–414. https://doi.org/10.1144/petgeo2018-152.

Branney, M.J., Kokelaar, B.P., 2002. Pyroclastic density currents and the sedimentation of ignimbrites. Geol. Soc. Lond. 27, 159. https://doi.org/10.1144/GSL.MEM.2003.0.

Brown, R.W., Beucher, R., Roper, S., Persano, C., Stuart, F., Fitzgerald, P., 2013. Natural age dispersion arising from the analysis of broken crystals. Part I: theoretical basis and implications for the apatite (U–Th)/He thermochronometer. Geochem. Cosmochim. Acta 122, 478–497. https://doi.org/10.1016/j.gca.2013.05.041.

Bustamante, C., Cardona, A., Bayona, G., Mora, A., Valencia, V., Gehrels, G., Vervoort, J., 2010. U-Pb LA-ICP-MS geochronology and regional correlation of middle jurassic intrusive rocks from the garzon massif, upper Magdalena Valley and central Cordillera, southern Colombia. Revista Boletín de Geología 32 (2). https://revistas.uis.edu.co/index.php/revistaboletindegeologia/article/view/2086.

Bustamante, C., Archanjo, C.J., Cardona, A., Vervoort, J.D., 2016. Late Jurassic to Early Cretaceous plutonism in the Colombian Andes: a record of long-term arc maturity. Geol. Soc. Am. Bull. 128 (11–12), 1762–1779. https://doi.org/10.1130/b31307.1.

Bustamante, C., Cardona, A., Archanjo, C.J., Bayona, G., Lara, M., Valencia, V., 2017. Geochemistry and isotopic signatures of Paleogene plutonic and detrital rocks of the Northern Andes of Colombia: a record of post-collisional arc magmatism. Lithos 277, 199–209. https://doi.org/10.1016/j.lithos.2016.11.025.

Butler, K., Schamel, S., 1988. Structure along the eastern margin of the central Cordillera, upper Magdalena Valley, Colombia. J. S. Am. Earth Sci. 1 (1), 109–120. https://doi.org/10.1016/0895-9811(88)90019-3.

Cardozo, N., Allmendinger, R.W., 2013. Spherical projections with OSXStereonet. Comput. Geosci. 51, 193–205. https://doi.org/10.1016/j.cageo.2012.07.021.

Carvajal-Torres, J., Catuneanu, O., Mora, A., Caballero, V., Reyes, M., 2022. First-order stratigraphic boundaries of the Late Cretaceous–Paleogene retroarc foreland basin in Colombia. Front. Earth Sci. 10 https://doi.org/10.3389/feart.2022.876140.

Cawood, A.J., Watkins, H., Bond, C.E., Warren, M.J., Cooper, M.A., 2023. Scaling of natural fracture patterns at Swift anticline, NW Montana: the influence of structural position, lithology, and observation scale. EGUsphere 1–36. https://doi.org/10.5194/egusphere-2023-812.

Cazier, E.C., Hayward, A.B., Espinosa, G., Velandia, J., Mugniot, J.-F., Leel Jr., W.G., 1995. Petroleum geology of the Cusiana field, Llanos Basin Foothills, Colombia. AAPG (Am. Assoc. Pet. Geol.) Bull. 79 https://doi.org/10.1306/7834d9fe-1721-11d7-8645000102c1865d.

Cediel, F., Mojica, J., Macia, C., 1980. Definición estratigráfica del Triásico en Colombia, Suramerica; formaciones Luisa, Payandé y Saldaña. Newsl. Stratigr. 9 (2), 73–104. https://doi.org/10.1127/nos/9/1980/73.

Celestino, M.A.L., Miranda, T. S. de, Mariano, G., Alencar, M. de L., Carvalho, B. R. B. M. de, Falcão, T. da C., Topan, J.G., Barbosa, J.A., Gomes, I.F., 2020. Fault damage zones width: implications for the tectonic evolution of the northern border of the Araripe Basin, Brazil, NE Brazil. J. Struct. Geol. 138, 104116 https://doi.org/10.1016/j.jsg.2020.104116.

Choi, J.-H., Edwards, P., Ko, K., Kim, Y.-S., 2016. Definition and classification of fault damage zones: a review and a new methodological approach. Earth Sci. Rev. 152, 70–87. https://doi.org/10.1016/j.earscirev.2015.11.006.

Cianfarra, P., Salvini, F., 2015. Lineament domain of regional strike-slip corridor: insight from the Neogene transtensional DE Geer transform fault in NW Spitsbergen. Pure Appl. Geophys. 172 (5), 1185–1201. https://doi.org/10.1007/s00024-014-0869-9.

Cooke, M.L., 1997. Predicting fracture localization in folded strata from mechanical stratigraphy and fold shape: case study of east Kaibab Monocline, Utah. Int. J. Rock Mech. Min. Sci. 34 (3–4), 56.e1–56.e12. https://doi.org/10.1016/s1365-1609(97)00248-7.

Cooper, M.A., Addison, F.T., Alvarez, R., Coral, M., Graham, R.H., Hayward, A.B., Howe, S., Martinez, J., Naar, J., Peñas, R., Pulham, A.J., Taborda, A., 1995. Basin development and tectonic history of the Llanos Basin, estern Cordillera, and middle Magdalena Valley, Colombia. AAPG (Am. Assoc. Pet. Geol.) Bull. 79 (10), 1421–1442. https://doi.org/10.1306/7834D9F4-1721-11D7-8645000102C1865D.

Cuong, T.X., Warren, J.K., 2009. Bach Ho field, a fractured granitic basement reservoir, Cuu Long Basin, offshore SE Vietnam: a "buried-hill" play. J. Petrol. Geol. 32 (2), 129–156. https://doi.org/10.1111/j.1747-5457.2009.00440.x.

Dashti, R., Rahimpour-Bonab, H., 2022. The effect of mechanical stratigraphy on natural fractures morphology and distribution in carbonate reservoirs. J. Petrol. Sci. Eng. 217 (110915), 110915 https://doi.org/10.1016/j.petrol.2022.110915.

de Freitas, M.G., 2000. The Saldaña victims. Unsuccessful Subthrust Exploration in the Upper Magdalena Valley of Colombia-Reasons for Failures and the Way Ahead.

Debenham, N., Farrell, N.J.C., Holford, S.P., King, R.C., Healy, D., 2019. Spatial distribution of micrometre-scale porosity and permeability across the damage zone of a reverse-reactivated normal fault in a tight sandstone: insights from the Otway Basin, SE Australia. Basin Res. 31 (3), 640–658. https://doi.org/10.1111/bre.12345.

Diederix, H., Bohórquez, O.P., Mora–Páez, H., Peláez, J.R., Cardona, L., Corchuelo, Y., Ramírez, J., Díaz–Mila, F., 2020. The Algeciras Fault System of the upper Magdalena Valley, huila department. Quaternary. In: Gómez, J., Pinilla–Pachon, A.O. (Eds.), The Geology of Colombia, vol. 4, pp. 423–452. https://doi.org/10.32685/pub.esp.38.2019.12. Servicio Geológico Colombiano, Publicaciones Geológicas Especiales 38.

Dimmen, V., Rotevatn, A., Peacock, D.C.P., Nixon, C.W., Nærland, K., 2017. Quantifying structural controls on fluid flow: insights from carbonate-hosted fault damage zones on the Maltese Islands. J. Struct. Geol. 101, 43–57. https://doi.org/10.1016/j.jsg.2017.05.012.

Espitia, W., Cortés, M., Beltrán, W., Higuera Díaz, I.C., Arias, J., 2022. Structural styles of the upper Magdalena Valley, northern Andes, Colombia: case studies. In: Zamora, G., Mora, A. (Eds.), Andean Structural Styles. Elsevier, pp. 139–148.

Etayo-Serna, F., Carrillo, G., 1996. Bioestratigrafía del Cretácico mediante macrofósiles en la sección el Ocal, Valle Superior del Magdalena, Colombia. Geol. Colomb. 20, 81–92.

Farley, K.A., 2002. (U-Th)/he dating: techniques, calibrations, and applications. Rev. Mineral. Geochem. 47 (1), 819–844. https://doi.org/10.2138/rmg.2002.47.18.

Ferrill, D.A., Morris, A.P., McGinnis, R.N., Smart, K.J., Wigginton, S.S., Hill, N.J., 2017. Mechanical stratigraphy and normal faulting. J. Struct. Geol. 94, 275–302. https://doi.org/10.1016/j.jsg.2016.11.010.

Flowers, R.M., Ketcham, R.A., Shuster, D.L., Farley, K.A., 2009. Apatite (U–Th)/He thermochronometry using a radiation damage accumulation and annealing model. Geochem. Cosmochim. Acta 73 (8), 2347–2365. https://doi.org/10.1016/j.gca.2009.01.015.

Folk, R.L., 1980. Petrology of Sedimentary Rocks. Hemphill publishing company.

Forstner, S.R., Laubach, S.E., 2022. Scale-dependent fracture networks. J. Struct. Geol. 165 (104748), 104748 https://doi.org/10.1016/j.jsg.2022.104748.

Gallagher, K., 2012. Transdimensional inverse thermal history modeling for quantitative thermochronology. J. Geophys. Res. 117 (B2) https://doi.org/10.1029/2011jb008825.

Gómez, E., Jordan, T.E., Allmendinger, R.W., Hegarty, K., Kelley, S., Heizler, M., 2003. Controls on architecture of the Late Cretaceous to Cenozoic southern Middle Magdalena Valley Basin, Colombia. Geol. Soc. Am. Bull. 115, 131–147. https://doi.org/10.1130/0016-7606(2003)115<0131:coaotl>2.0.co;2.

Gómez, E., Jordan, T.E., Allmendinger, R.W., Hegarty, K., Kelley, S., 2005. Syntectonic cenozoic sedimentation in the northern middle Magdalena Valley Basin of Colombia and implications for exhumation of the northern Andes. Geol. Soc. Am. Bull. 117 (5), 547. https://doi.org/10.1130/b25454.1.

Gómez, J., Montes, N.E., 2020. Mapa Geológico de Colombia en Relieve 2020. In: Escala 1:1 000 000, 2 hojas. Servicio Geológico Colombiano, Bogotá.

Green, P.F., Duddy, I.R., Gleadow, A.J.W., Tingate, P.R., Laslett, G.M., 1985. Fission-track annealing in apatite: track length measurements and the form of the Arrhenius plot. Int. J. Radiat. Appl. Instrum. Nucl. Tracks Radiat. Meas. 10 (3), 323–328. https://doi.org/10.1016/0735-245x(85)90121-8.

Green, P.F., Duddy, I.R., Gleadow, A.J.W., Tingate, P.R., Laslett, G.M., 1986. Thermal annealing of fission tracks in apatite. Chem. Geol. 59, 237–253. https://doi.org/10.1016/0168-9622(86)90074-6.

Guenthner, W.R., Reiners, P.W., Ketcham, R.A., Nasdala, L., Giester, G., 2013. Helium diffusion in natural zircon: radiation damage, anisotropy, and the interpretation of zircon (U-Th)/He thermochronology. Am. J. Sci. 313 (3), 145–198. https://doi.org/10.2475/03.2013.01.

Guerrero, J., Montes, L., Jaillard, E., Kammer, A., 2021. Seismic interpretation of the cretaceous unconformities and sequences in the middle Magdalena Valley and the western margin of the eastern Cordillera, Colombia. Compt. Rendus Geosci. 353 (1), 155–172. https://doi.org/10.5802/crgeos.47.

Hansberry, R.L., King, R.C., Holford, S.P., Hand, M., Debenham, N., 2021. How wide is a fault damage zone? Using network topology to examine how fault-damage zones overprint regional fracture networks. J. Struct. Geol. 146 (104327), 104327 https://doi.org/10.1016/j.jsg.2021.104327.

Harrison, T.M., 2005. Fundamentals of noble gas thermochronometry. Rev. Mineral. Geochem. 58 (1), 123–149. https://doi.org/10.2138/rmg.2005.58.5.

Hooker, J.N., Katz, R.F., 2015. Vein spacing in extending, layered rock: the effect of synkinematic cementation. Am. J. Sci. 315 (6), 557–588. https://doi.org/10.2475/06.2015.03.

Hooker, J.N., Laubach, S.E., Gomez, L., Marrett, R., Eichhubl, P., Diaz-Tushman, K., Pinzon, E., 2011. Fracture size, frequency, and strain in the Cambrian Eriboll formation sandstones, NW Scotland. Scot. J. Geol. 47 (1), 45–56. https://doi.org/10.1144/0036-9276/01-420.

Hooker, J.N., Laubach, S.E., Marrett, R., 2013. Fracture-aperture size—frequency, spatial distribution, and growth processes in strata-bounded and non-strata-bounded fractures, Cambrian Mesón Group, NW Argentina. J. Struct. Geol. 54, 54–71. https://doi.org/10.1016/j.jsg.2013.06.011.

Hooker, J.N., Laubach, S.E., Marrett, R., 2018. Microfracture spacing distributions and the evolution of fracture patterns in sandstones. J. Struct. Geol. 108, 66–79. https://doi.org/10.1016/j.jsg.2017.04.001.

Horton, B.K., Parra, M., Mora, A., 2020. Construction of the eastern Cordillera of Colombia: insights from the sedimentary record. In: Gómez, J., Mateus–Zabala, D. (Eds.), The Geology of Colombia: Vol. 3 Paleogene – Neogene, vol. 37. Servicio Geológico Colombiano, Publicaciones Geológicas Especiales, pp. 67–88. https://doi.org/10.32685/pub.esp.37.2019.03.

Jaimes, E., de Freitas, M., 2006. An Albian–Cenomanian unconformity in the northern Andes: evidence and tectonic significance. J. S. Am. Earth Sci. 21 (4), 466–492. https://doi.org/10.1016/j.jsames.2006.07.011.

Jiang, F., Cheng, R., Ruan, B., Lin, B., Xu, Z., Li, Z., 2017. Formation mechanism of volcanic reservoirs within a volcanostratigraphic framework: the case of the Wangfu fault depression in the Songliao Basin, China. Mar. Petrol. Geol. 84, 160–178. https://doi.org/10.1016/j.marpetgeo.2017.03.036.

Jiménez, G., Rico, J., Bayona, G., Montes, C., Rosero, A., Sierra, D., 2012. Analysis of curved folds and fault/fold terminations in the southern Upper Magdalena Valley of Colombia. J. S. Am. Earth Sci. 39, 184–201. https://doi.org/10.1016/j.jsames.2012.04.006.

Kellogg, J.N., Vega, V., 1995. Tectonic development of Panama, Costa Rica, and the Colombian Andes: constraints from global positioning system geodetic studies and gravity. Geol. Soc. Am. Special Paper 295, 75–90. https://doi.org/10.1130/SPE295-p75.

Ketcham, R.A., Carter, A., Donelick, R.A., Barbarand, J., Hurford, A.J., 2007. Improved modeling of fission-track annealing in apatite. Am. Mineral. 92 (5–6), 799–810. https://doi.org/10.2138/am.2007.2281.

Kim, Y.-S., Peacock, D.C.P., Sanderson, D.J., 2004. Fault damage zones. J. Struct. Geol. 26 (3), 503–517. https://doi.org/10.1016/j.jsg.2003.08.002.

Koning, T., 2019. Exploring in Asia, Africa and the Americas for oil and gas in naturally fractured basement reservoirs: best practices and lessons learned. Georesursy 21 (4), 10–18. https://doi.org/10.18599/grs.2019.4.10-18.

Laubach, Stephen E., Olson, J.E., Gale, J.F.W., 2004. Are open fractures necessarily aligned with maximum horizontal stress? Earth Planet Sci. Lett. 222 (1), 191–195. https://doi.org/10.1016/j.epsl.2004.02.019.

Laubach, S.E., Olson, J.E., Gross, M.R., 2009. Mechanical and fracture stratigraphy. AAPG (Am. Assoc. Pet. Geol.) Bull. 93 (11), 1413–1426. https://doi.org/10.1306/07270909094.

Laubach, S.E., Eichhubl, P., Hargrove, P., Ellis, M.A., Hooker, J.N., 2014. Fault core and damage zone fracture attributes vary along strike owing to interaction of fracture growth, quartz accumulation, and differing sandstone composition. J. Struct. Geol. 68, 207–226. https://doi.org/10.1016/j.jsg.2014.08.007.

Laubach, S.E., Lander, R.H., Criscenti, L.J., Anovitz, L.M., Urai, J.L., Pollyea, R.M., Hooker, J.N., Narr, W., Evans, M.A., Kerisit, S.N., Olson, J.E., Dewers, T., Fisher, D., Bodnar, R., Evans, B., Dove, P., Bonnell, L.M., Marder, M.P., Pyrak-Nolte, L., 2019. The role of chemistry in fracture pattern development and opportunities to advance interpretations of geological materials. Rev. Geophys. 57 (3), 1065–1111. https://doi.org/10.1029/2019rg000671.

Le Maitre, R.W. (Ed.), 2002. Igneous Rocks: A Classification and Glossary of Terms: Recommendations of the International Union of Geological Sciences Subcommission on the Systematics of Igneous Rocks, second ed. Cambridge University Press.

Leal-Mejía, H., Shaw, R.P., Melgarejo i Draper, J.C., 2019. Spatial-temporal migration of granitoid magmatism and the Phanerozoic tectono-magmatic evolution of the Colombian Andes. In: Geology and Tectonics of Northwestern South America. Springer International Publishing, pp. 253–410.

Li, Y., Hou, G., Hari, K.R., Neng, Y., Lei, G., Tang, Y., Zhou, L., Sun, S., Zheng, C., 2018. The model of fracture development in the faulted folds: the role of folding and faulting. Mar. Petrol. Geol. 89, 243–251. https://doi.org/10.1016/j.marpetgeo.2017.05.025.

Li, L., Li, C., Huang, B., Wang, M., Bai, Z., Qi, S., 2022. Influence of the welding degree on the strength and failure modes of Tuff. Materials 15 (24), 8757. https://doi.org/10.3390/ma15248757.

Lin, A., Yamashita, K., 2013. Spatial variations in damage zone width along strike-slip faults: an example from active faults in southwest Japan. J. Struct. Geol. 57, 1–15. https://doi.org/10.1016/j.jsg.2013.10.006.

Lisle, R.J., 1994. Detection of zones of abnormal strains in structures using Gaussian curvature analysis. AAPG (Am. Assoc. Pet. Geol.) Bull. 78 (12), 1811–1819. https://doi.org/10.1306/a25ff305-171b-11d7-8645000102c1865d.

Ma, S., Zeng, L., Tian, H., Shi, X., Wu, W., Yang, S., Luo, L., Xu, X., 2023. Fault damage zone and its effect on deep shale gas: insights from 3D seismic interpretation in the southern Sichuan Basin, China. J. Struct. Geol. 170 (104848), 104848 https://doi.org/10.1016/j.jsg.2023.104848.

Malusà, M.G., Fitzgerald, P.G., 2019. Application of thermochronology to geologic problems: bedrock and detrital approaches. In: Fission-Track Thermochronology and its Application to Geology. Springer International Publishing, pp. 191–209.

Manniello, C., Agosta, F., Todaro, S., Cavalcante, F., Prosser, G., 2022. Fracture stratigraphy of Mesozoic platform carbonates, Agri Valley, southern Italy. Geol. Mag. 159 (11–12), 1–23. https://doi.org/10.1017/s0016756822000322.

Marrett, R., 1996. Aggregate properties of fracture populations. J. Struct. Geol. 18 (2–3), 169–178. https://doi.org/10.1016/s0191-8141(96)80042-3.

Mauldon, M., Dunne, W.M., Rohrbaugh Jr., M.B., 2001. Circular scanlines and circular windows: new tools for characterizing the geometry of fracture traces. J. Struct. Geol. 23 (2–3), 247–258. https://doi.org/10.1016/s0191-8141(00)00094-8.

McPhie, J., Doyle, M., Allen, S.R., 1993. Volcanic textures: a guide to the interpretation of textures in volcanic rocks. Centre for Ore Deposit and Exploration Studies. University of Tasmania, p. 198.

Meng, Y., Chen, H., Luo, Y., Zhao, Y., Tang, D., He, F., 2023. Architecture of intraplate strike-slip fault zones in the Yanchang Formation, Southern Ordos Basin, China: characterization and implications for their control on hydrocarbon enrichment. J. Struct. Geol. 170 (104851), 104851 https://doi.org/10.1016/j.jsg.2023.104851.

Mojica, J., Llinás, R., 1984. Observaciones recientes sobre las caracteristicas del basamento economico del Valle Superior del Magdalena en la region de Payandé-Rovira (Tolima, Colombia), y en especial sobre la estratigrafía y petrografía del Miembro Chicalá (parte baja de la Fm. Saldañaa). Geol. Colomb. 13, 81–128.

Montes, C., Rodriguez-Corcho, A.F., Bayona, G., Hoyos, N., Zapata, S., Cardona, A., 2019. Continental margin response to multiple arc-continent collisions: the northern Andes-Caribbean margin. Earth Sci. Rev. 198 (102903), 102903 https://doi.org/10.1016/j.earscirev.2019.102903.

Mora, A., Parra, M., Strecker, M.R., Kammer, A., Dimaté, C., Rodríguez, F., 2006. Cenozoic contractional reactivation of Mesozoic extensional structures in the Eastern Cordillera of Colombia. Tectonics 25 (2). https://doi.org/10.1029/2005tc001854.

Mora, A., Gaona, T., Kley, J., Montoya, D., Parra, M., Quiroz, L.I., Reyes, G., Strecker, M. R., 2009. The role of inherited extensional fault segmentation and linkage in contractional orogenesis: a reconstruction of Lower Cretaceous inverted rift basins in the Eastern Cordillera of Colombia. Basin Res. 21 (1), 111–137. https://doi.org/10.1111/j.1365-2117.2008.00367.x.

Mora, A., Mantilla, M., De Freitas, M., 2010. Cretaceous Paleogeography and Sedimentation in the Upper Magdalena and Putumayo Basins, Southwestern Colombia, vol. 50246. Search and Discovery Article, pp. 15–18.

Mora, A., Reyes-Harker, A., Rodriguez, G., Tesón, E., Ramirez-Arias, J.C., Parra, M., Caballero, V., Mora, J.P., Quintero, I., Valencia, V., Ibañez, M., Horton, B.K., Stockli, D.F., 2013. Inversion tectonics under increasing rates of shortening and sedimentation: Cenozoic example from the Eastern Cordillera of Colombia. Geol. Soc. Spec. Publ. 377 (1), 411–442. https://doi.org/10.1144/sp377.6.

Mora, A., Villagómez, D., Parra, M., Caballero, V.M., Spikings, R., Horton, B.K., Mora–Bohórquez, J.A., Ketcham, R.A., Arias–Martínez, J.P., 2020. Late cretaceous to Cenozoic uplift of the northern Andes: paleogeographic implications. In: Gómez, J., Mateus–Zabala, D. (Eds.), The Geology of Colombia: Vol. 3 Paleogene – Neogene, vol. 37. Servicio Geológico Colombiano, Publicaciones Geológicas Especiales, pp. 89–121.

Mora-Páez, H., Kellogg, J.N., Freymueller, J.T., Mencin, D., Fernandes, R.M.S., Diederix, H., LaFemina, P., Cardona-Piedrahita, L., Lizarazo, S., Peláez-Gaviria, J.-R., Díaz-Mila, F., Bohórquez-Orozco, O., Giraldo-Londoño, L., Corchuelo-Cuervo, Y., 2019. Crustal deformation in the northern Andes – a new GPS velocity field. J. S. Am. Earth Sci. 89, 76–91. https://doi.org/10.1016/j.jsames.2018.11.002.

Mousavi, M.A., Bryant, S.L., 2013. Geometric models of porosity reduction by ductile grain compaction and cementation. AAPG (Am. Assoc. Pet. Geol.) Bull. 97 (12), 2129–2148. https://doi.org/10.1306/05171311165.

Murray, K.E., Orme, D.A., Reiners, P.W., 2014. Effects of U–Th-rich grain boundary phases on apatite helium ages. Chem. Geol. 390, 135–151. https://doi.org/10.1016/j.chemgeo.2014.09.023.

Nelson, R.A., Serra, S., 1995. Vertical and lateral variations in fracture spacing in folded carbonate sections and its relation to locating horizontal wells. J. Can. Petrol. Technol. 34 (6) https://doi.org/10.2118/95-06-05.

Nyberg, B., Nixon, C.W., Sanderson, D.J., 2018. NetworkGT: a GIS tool for geometric and topological analysis of two-dimensional fracture networks. Geosphere 14 (4), 1618–1634. https://doi.org/10.1130/GES01595.1.

Olson, J.E., 2004. Predicting fracture swarms — the influence of subcritical crack growth and the crack-tip process zone on joint spacing in rock. Geol. Soc. Spec. Publ. 231 (1), 73–88. https://doi.org/10.1144/gsl.sp.2004.231.01.05.

Ortega, O.J., Marrett, R.A., Laubach, S.E., 2006. A scale-independent approach to fracture intensity and average spacing measurement. AAPG (Am. Assoc. Pet. Geol.) Bull. 90 (2), 193–208. https://doi.org/10.1306/08250505059.

Ortega, O.J., Gale, J.F.W., Marrett, R., 2010. Quantifying diagenetic and stratigraphic controls on fracture intensity in platform carbonates: an example from the Sierra

Madre Oriental, northeast Mexico. J. Struct. Geol. 32 (12), 1943–1959. https://doi.org/10.1016/j.jsg.2010.07.004.
Parra, M., Mora, A., Lopez, C., Ernesto Rojas, L., Horton, B.K., 2012. Detecting earliest shortening and deformation advance in thrust belt hinterlands: example from the Colombian Andes. Geology 40 (2), 175–178. https://doi.org/10.1130/g32519.1.
Patiño, A.M., Parra, M., Ramírez, J.C., Sobel, E.R., Glodny, J., Almendral, A., Echeverri, S., 2019. Thermochronological constraints on Cenozoic exhumation along the southern Caribbean: the Santa Marta range, northern Colombia. In: Andean Tectonics. Elsevier, pp. 103–132.
Peacock, D.C.P., Dimmen, V., Rotevatn, A., Sanderson, D.J., 2017a. A broader classification of damage zones. J. Struct. Geol. 102, 179–192. https://doi.org/10.1016/j.jsg.2017.08.004.
Peacock, D.C.P., Nixon, C.W., Rotevatn, A., Sanderson, D.J., Zuluaga, L.F., 2017b. Interacting faults. J. Struct. Geol. 97, 1–22. https://doi.org/10.1016/j.jsg.2017.02.008.
Peacock, D.C.P., Sanderson, D.J., Rotevatn, A., 2018. Relationships between fractures. J. Struct. Geol. 106, 41–53. https://doi.org/10.1016/j.jsg.2017.11.010.
Pérez-Consuegra, N., Hoke, G.D., Mora, A., Fitzgerald, P., Sobel, E.R., Sandoval, J.R., Glodny, J., Valencia, V., Parra, M., Zapata, S., 2021. The case for tectonic control on erosional exhumation on the tropical northern Andes based on thermochronology data. Tectonics 40 (4). https://doi.org/10.1029/2020tc006652.
Priest, S.D., Hudson, J.A., 1981. Estimation of discontinuity spacing and trace length using scanline surveys. Int. J. Rock Mech. Min. Sci. Geomech. Abstracts 18 (3), 183–197. https://doi.org/10.1016/0148-9062(81)90973-6.
Rahiman, T.I.H., Pettinga, J.R., 2008. Analysis of lineaments and their relationship to Neogene fracturing, SE Viti Levu, Fiji. Geol. Soc. Am. Bull. 120 (11–12), 1544–1555. https://doi.org/10.1130/B26264.1.
Ramon, J.C., Rosero, A., 2006. Multiphase structural evolution of the western margin of the Girardot subbasin, Upper Magdalena Valley, Colombia. J. S. Am. Earth Sci. 21 (4), 493–509. https://doi.org/10.1016/j.jsames.2006.07.012.
Rashid, F., Hussein, D., Lorinczi, P., Glover, P.W.J., 2023. The effect of fracturing on permeability in carbonate reservoir rocks. Mar. Petrol. Geol. 152 (106240), 106240 https://doi.org/10.1016/j.marpetgeo.2023.106240.
Reiners, P.W., 2005. Past, present, and future of thermochronology. Rev. Mineral. Geochem. 58 (1), 1–18. https://doi.org/10.2138/rmg.2005.58.1.
Restrepo, M., Bustamante, C., Cardona, A., Beltrán-Triviño, A., Bustamante, A., Chavarría, L., Valencia, V.A., 2021. Tectonic implications of the jurassic magmatism and the metamorphic record at the southern Colombian Andes. J. S. Am. Earth Sci. 111 (103439), 103439 https://doi.org/10.1016/j.jsames.2021.103439.
Restrepo-Moreno, S., Foster, D., Stockli, D., Parra-Sánchez, L., 2009. Long-term erosion and exhumation of the "altiplano Antioqueño" (1–2), 1–12. In: Northern Andes (Colombia) from apatite (U–Th)/He thermochronology. Earth and Planetary Science Letters, 278 https://doi.org/10.1016/j.epsl.2008.09.037.
Reyes-Harker, A., Ruiz-Valdivieso, C.F., Mora, A., Ramírez-Arias, J.C., Rodriguez, G., de la Parra, F., Caballero, V., Parra, M., Moreno, N., Horton, B.K., Saylor, J.E., Silva, A., Valencia, V., Stockli, D., Blanco, V., 2015. Hyperspectral imaging for the determination of bitumen content in Athabasca oil sands core samples. AAPG (Am. Assoc. Pet. Geol.) Bull. 99 (8), 1407–1453. https://doi.org/10.1306/06181411110.
Rodríguez, G., Arango, M.I., Zapata, G., G, Bermúdez, J.G., 2016. Catálogo de unidades litoestratigráficas de Colombia - Formación Saldaña - Cordilleras Central y Oriental Tolima, Huila, Cauca y Putumayo. Catálogos Estratigráficos Servicio Geológico Colombiano 91.
Rodríguez, G., Arango, M.I., Zapata, G., Bermúdez, J.G., 2018. Petrotectonic characteristics, geochemistry, and U-Pb geochronology of Jurassic plutons in the Upper Magdalena Valley-Colombia: implications on the evolution of magmatic arcs in the NW Andes. J. S. Am. Earth Sci. 81, 10–30. https://doi.org/10.1016/j.jsames.2017.10.012.
Rodríguez–García, G., Correa–Martínez, A.M., Zapata–García, G., Arango–Mejía, M.I., Obando–Erazo, G., Zapata–Villada, J.P., Bermúdez, J.G., 2020. Diverse Jurassic magmatic arcs of the Colombian Andes: constraints from petrography, geochronology, and geochemistry. In: Gómez, J., Pinilla–Pachon, A.O. (Eds.), The Geology of Colombia, 2 Mesozoic, pp. 117–170. https://doi.org/10.32685/pub.esp.36.2019.04. Servicio Geológico Colombiano, Publicaciones Geológicas Especiales 36.
Rohrbaugh Jr., M.B., Dunne, W.M., Mauldon, M., 2002. Estimating fracture trace intensity, density, and mean length using circular scan lines and windows. AAPG (Am. Assoc. Pet. Geol.) Bull. 86 (12), 2089–2104. https://doi.org/10.1306/61EEDE0E-173E-11D7-8645000102C1865D.
Roncancio, J., Martínez, M., 2011. Upper Magdalena basin. In: Cediel, F., Colmenares, F. (Eds.), Petroleum Geology of Colombia, vol. 14. Fondo Editorial Universidad EAFIT.
Rosero, A., Carrero, M., Ceballos, C., Mora, A., 2022. Seismic and structural analysis of the San Francisco oil field (Colombia). Structural controls on a complex hydrocarbon charge history. In: Andean Structural Styles. Elsevier, pp. 195–206.
Saeid, E., Bakioglu, K.B., Kellogg, J., Leier, A., Martinez, J.A., Guerrero, E., 2017. Garzón Massif basement tectonics: structural control on evolution of petroleum systems in upper Magdalena and Putumayo basins, Colombia. Mar. Petrol. Geol. 88, 381–401. https://doi.org/10.1016/j.marpetgeo.2017.08.035.
Saein, A.F., Riahi, Z.T., 2019. Controls on fracture distribution in Cretaceous sedimentary rocks from the Isfahan region, Iran. Geol. Mag. 156 (6), 1092–1104. https://doi.org/10.1017/s0016756817000346.
Sánchez-Villar, N., Kammer, A., Cárdenas, J., Mora, A., Tamara, J., 2011. Significado de fracturas en la evolución estructural del Anticlinal de Monterralo, Piedemonte Llanero, Cordillera Oriental de Colombia. Geol. Colomb. 36, 105–122. https://revistas.unal.edu.co/index.php/geocol/article/view/22675.
Sanderson, D.J., Nixon, C.W., 2015. The use of topology in fracture network characterization. J. Struct. Geol. 72, 55–66. https://doi.org/10.1016/j.jsg.2015.01.005.
Sanderson, D.J., Nixon, C.W., 2018. Topology, connectivity and percolation in fracture networks. J. Struct. Geol. 115, 167–177. https://doi.org/10.1016/j.jsg.2018.07.011.
Sarmiento, L.F., Rangel, A., 2004. Petroleum systems of the upper Magdalena valley, Colombia. Mar. Petrol. Geol. 21 (3), 373–391. https://doi.org/10.1016/j.marpetgeo.2003.11.019.
Sarmiento-Rojas, L.F., 2019. Cretaceous stratigraphy and Paleo-facies maps of northwestern south America. In: Geology and Tectonics of Northwestern South America. Springer International Publishing, pp. 673–747.
Sarmiento-Rojas, L.F., Van Wess, J.D., Cloetingh, S., 2006. Mesozoic transtensional basin history of the Eastern Cordillera, Colombian Andes: inferences from tectonic models. J. S. Am. Earth Sci. 21 (4), 383–411. https://doi.org/10.1016/j.jsames.2006.07.003.
Shuster, D.L., Flowers, R.M., Farley, K.A., 2006. The influence of natural radiation damage on helium diffusion kinetics in apatite. Earth Planet Sci. Lett. 249 (3–4), 148–161. https://doi.org/10.1016/j.epsl.2006.07.028.
Siravo, G., Faccenna, C., Gérault, M., Becker, T.W., Fellin, M.G., Herman, F., Molin, P., 2019. Slab flattening and the rise of the eastern Cordillera, Colombia. Earth Planet Sci. Lett. 512, 100–110. https://doi.org/10.1016/j.epsl.2019.02.002.
Sobel, E.R., Strecker, M.R., 2003. Uplift, exhumation and precipitation: tectonic and climatic control of Late Cenozoic landscape evolution in the northern Sierras Pampeanas, Argentina: uplift, exhumation, and precipitation in the Sierras Pampeanas. Basin Res. 15 (4), 431–451. https://doi.org/10.1046/j.1365-2117.2003.00214.x.
Spikings, R., Cochrane, R., Villagómez, D., Van der Lelij, R., Vallejo, C., Winkler, W., Beate, B., 2015. The geological history of northwestern South America: from pangaea to the early collision of the Caribbean large igneous province (290–75Ma). Gondwana Res.: Int. Geosci. J. 27 (1), 95–139. https://doi.org/10.1016/j.gr.2014.06.004.
Sun, H., Zhong, D., 2018. Origin and forming process of the porosity in volcanic hydrocarbon reservoirs of China. J. Volcanol. Geoth. Res. 350, 61–68. https://doi.org/10.1016/j.jvolgeores.2017.12.005.
Sun, X., Gomez-Rivas, E., Alcalde, J., Martín-Martín, J.D., Ma, C., Muñoz-López, D., Cruset, D., Cantarero, I., Griera, A., Travé, A., 2021. Fracture distribution in a folded fluvial succession: the Puig-reig anticline (south-eastern Pyrenees). Mar. Petrol. Geol. 132 (105169), 105169 https://doi.org/10.1016/j.marpetgeo.2021.105169.
Suttner, L.J., Basu, A., Mack, G.H., 1981. Climate and the origin of quartz arenites. J. Sediment. Res. 51 (4), 1235–1246. https://doi.org/10.1306/212F7E73-2B24-11D7-8648000102C1865D.
Taboada, A., Rivera, L.A., Fuenzalida, A., Cisternas, A., Philip, H., Bijwaard, H., Olaya, J., Rivera, C., 2000. Geodynamics of the northern Andes: Subductions and intracontinental deformation (Colombia). Tectonics 19 (5), 787–813. https://doi.org/10.1029/2000TC900004.
Tamara, J., Mora, A., Robles, W., Kammer, A., Ortiz, A., Sanchez-Villar, N., Piraquive, A., Rueda, L.H., Casallas, W., Castellanos, J., Montaña, J., Parra, L.G., Corredor, J., Ramirez, Á., Zambrano, E., 2015. Fractured reservoirs in the Eastern Foothills, Colombia, and their relationship with fold kinematics. AAPG (Am. Assoc. Pet. Geol.) Bull. 99 (8), 1599–1633. https://doi.org/10.1306/09291411109.
Tang, H., Tian, Z., Gao, Y., Dai, X., 2022. Review of volcanic reservoir geology in China. Earth Sci. Rev. 232 (104158), 104158 https://doi.org/10.1016/j.earscirev.2022.104158.
Tiab, D., Donaldson, E.C., 2015. Petrophysics: Theory and Practice of Measuring Reservoir Rock and Fluid Transport Properties, fourth ed. Gulf Professional Publishing.
Todaro, S., Agosta, F., Parrino, N., Cavalcante, F., Di Stefano, P., Giarrusso, R., Pepe, F., Renda, P., Tondi, E., 2022. Fracture stratigraphy and oil first migration in Triassic shales, Favignana Island, western Sicily, Italy. Mar. Petrol. Geol. 135 (105400), 105400 https://doi.org/10.1016/j.marpetgeo.2021.105400.
Trenkamp, R., Kellogg, J.N., Freymueller, J.T., Mora, H.P., 2002. Wide plate margin deformation, southern Central America and northwestern South America, CASA GPS observations. J. South Am. Earth Sci. 15, 157–171. https://doi.org/10.1016/S0895-9811(02)00018-4.
Ukar, E., Laubach, S.E., Hooker, J.N., 2019. Outcrops as guides to subsurface natural fractures: example from the Nikanassin Formation tight-gas sandstone, Grande Cache, Alberta foothills, Canada. Mar. Petrol. Geol. 103, 255–275. https://doi.org/10.1016/j.marpetgeo.2019.01.039.
Velandia, F., Acosta, J., Terraza, R., Villegas, H., 2005. The current tectonic motion of the northern Andes along the Algeciras Fault System in SW Colombia. Tectonophysics 399 (1–4), 313–329. https://doi.org/10.1016/j.tecto.2004.12.028.
Villagómez, D., Spikings, R., 2013. Thermochronology and tectonics of the central and western cordilleras of Colombia: early Cretaceous–tertiary evolution of the northern Andes. Lithos 160–161, 228–249. https://doi.org/10.1016/j.lithos.2012.12.008.
Villagómez, D., Spikings, R., Magna, T., Kammer, A., Winkler, W., Beltrán, A., 2011. Geochronology, geochemistry and tectonic evolution of the Western and Central cordilleras of Colombia. Lithos 125 (3–4), 875–896. https://doi.org/10.1016/j.lithos.2011.05.003.
Villamizar-Escalante, N., Bernet, M., Urueña-Suárez, C., Hernández-González, J.S., Terraza-Melo, R., Roncancio, J., Muñoz-Rocha, J.A., Peña-Urueña, M.L., Amaya, S., Piraquive, A., 2021. Thermal history of the southern central Cordillera and its exhumation record in the cenozoic deposits of the upper Magdalena Valley, Colombia. J. S. Am. Earth Sci. 107 (103105), 103105 https://doi.org/10.1016/j.jsames.2020.103105.
Walter, B., Géraud, Y., Bartier, D., Kluska, J.-M., Diraison, M., Morlot, C., Raisson, F., 2018. Petrophysical and mineralogical evolution of weathered crystalline basement

in western Uganda: implications for fluid transfer and storage. AAPG (Am. Assoc. Pet. Geol.) Bull. 102 (6), 1035–1065. https://doi.org/10.1306/0810171610917171.
Wang, Q., Narr, W., Laubach, S.E., 2023. Quantitative characterization of fracture spatial arrangement and intensity in a reservoir anticline using horizontal wellbore image logs and an outcrop analogue. Mar. Petrol. Geol. 152 (106238), 106238 https://doi.org/10.1016/j.marpetgeo.2023.106238.
Watkins, H., Bond, C.E., Healy, D., Butler, R.W.H., 2015. Appraisal of fracture sampling methods and a new workflow to characterise heterogeneous fracture networks at outcrop. J. Struct. Geol. 72, 67–82. https://doi.org/10.1016/j.jsg.2015.02.001.
Watkins, H., Healy, D., Bond, C.E., Butler, R.W.H., 2018. Implications of heterogeneous fracture distribution on reservoir quality; an analogue from the Torridon Group sandstone, Moine Thrust Belt, NW Scotland. J. Struct. Geol. 108, 180–197. https://doi.org/10.1016/j.jsg.2017.06.002.
Wei, W., Zhu, X., Azmy, K., Zhu, S., He, M., Sun, S., 2020. Depositional and compositional controls on diagenesis of the mixed siliciclastic-volcaniclastic sandstones: a case study of the Lower Cretaceous in Erennaoer Sag, Erlian Basin, NE China. J. Petrol. Sci. Eng. 188 (106855), 106855 https://doi.org/10.1016/j.petrol.2019.106855.
Wei, W., Azmy, K., Zhu, X., 2022. Impact of diagenesis on reservoir quality of the lacustrine mixed carbonate-siliciclastic-volcaniclastic rocks in China. J. Asian Earth Sci. 233 (105265), 105265 https://doi.org/10.1016/j.jseaes.2022.105265.
Wen, L., Li, Y., Yi, H., Liu, X., Zhang, B., Qiu, Y., Zhou, G., Zhang, X., 2019. Lithofacies and reservoir characteristics of Permian volcanic rocks in the Sichuan Basin. Nat. Gas. Ind. B 6 (5), 452–462. https://doi.org/10.1016/j.ngib.2019.02.003.
Wennberg, O.P., Azizzadeh, M., Aqrawi, A.A.M., Blanc, E., Brockbank, P., Lyslo, K.B., Pickard, N., Salem, L.D., Svånå, T., 2007. The Khaviz Anticline: an outcrop analogue to giant fractured Asmari Formation reservoirs in SW Iran. Geol. Soc. Spec. Publ. 270 (1), 23–42. https://doi.org/10.1144/gsl.sp.2007.270.01.02.
Wise, D.U., Funiciello, R., Parotto, M., Salvini, F., 1985. Topographic lineament swarms: clues to their origin from domain analysis of Italy. Geol. Soc. Am. Bull. 96 (7), 952–967. https://doi.org/10.1130/0016-7606(1985)96<952:TLSCTT>2.0.CO;2.
Zapata, S., Sobel, E.R., del Papa, C., Jelinek, A.R., Glodny, J., 2019a. Using a paleosurface to constrain low-temperature thermochronological data: tectonic evolution of the Cuevas range, Central Andes. Tectonics 38 (11), 3939–3958. https://doi.org/10.1029/2019tc005887.
Zapata, S., Sobel, E.R., del Papa, C., Muruaga, C., Zhou, R., 2019b. Miocene fragmentation of the Central Andean foreland basins between 26 and 28°S. J. S. Am. Earth Sci. 94 (102238), 102238 https://doi.org/10.1016/j.jsames.2019.102238.
Zapata, S., Patiño, A., Cardona, A., Parra, M., Valencia, V., Reiners, P., Oboh-Ikuenobe, F., Genezini, F., 2020. Bedrock and detrital zircon thermochronology to unravel exhumation histories of accreted tectonic blocks: an example from the Western Colombian Andes. J. S. Am. Earth Sci. 103 (102715), 102715 https://doi.org/10.1016/j.jsames.2020.102715.
Zapata, S., Calderon-Diaz, L., Jaramillo, C., Oboh-Ikuenobe, F., Piedrahita, J.C., Rodríguez-Cuevas, M., Cardona, A., Sobel, E.R., Parra, M., Valencia, V., Patiño, A., Jaramillo-Rios, J.S., Flores, M., Glodny, J., 2023. Drainage and sedimentary response of the Northern Andes and the Pebas system to Miocene strike-slip tectonics: a source to sink study of the Magdalena Basin. Basin Res. https://doi.org/10.1111/bre.12769.
Zheng, H., Sun, X., Zhu, D., Tian, J., Wang, P., Zhang, X., 2018. Characteristics and factors controlling reservoir space in the Cretaceous volcanic rocks of the Hailar Basin, NE China. Mar. Petrol. Geol. 91, 749–763. https://doi.org/10.1016/j.marpetgeo.2018.01.038.
Zhou, Y., Ji, Y., Zhang, S., Wan, L., 2016. Controls on reservoir quality of lower cretaceous tight sandstones in the Laiyang sag, Jiaolai basin, eastern China: integrated sedimentologic, diagenetic and microfracturing data. Mar. Petrol. Geol. 76, 26–50. https://doi.org/10.1016/j.marpetgeo.2016.05.019.
Zou, C., 2017. Unconventional Petroleum Geology. Elsevier.